LBL--19663

DE85 013817

DISCLAIMER

DEVELOPMENT OF SMALL-DIAMETER LEAD-GLASS-TUBE MATRICES FOR GAMMA-RAY CONVERSION IN POSITRON EMISSION TOMOGRAPHY

Gary Michael Schwartz
M.S. Thesis

Lawrence Berkeley Laboratory
University of California
Berkeley, California 94720

May 1985

This work was support by the U.S. Department of Energy under Contract Number DE-AC03-76SF00098.

DEVELOPMENT OF SMALL-DIAMETER LEAD-GLASS-TUBE MATRICES FOR GAMMA-RAY CONVERSION IN POSITRON EMISSION TOMOGRAPHY

Gary Michael Schwartz

ABSTRACT

A gamma-ray converter for a multiwire proportional chamber (MWPC) positron emission tomograph is described. The converter is made of small-diameter (0.48 mm inner diameter, 0.06 mm wall thickness) lead-oxide-glass tubes fused to form a honeycomb matrix. The surfaces of the tubes are reduced in a hydrogen atmosphere to provide the drift electric field for detection of the conversion electrons. The detection efficiency for a 10 mm thick converter is 6.65%, with a time resolution of 160 ns (FWHM). A scheme which will improve the spatial resolution of the tomograph by use of the self quenching streamer mode of chamber operation is described. Details of construction of the converters and the MWPC are presented, as well as the design performance of a high spatial resolution positron emission tomograph (HISPET).

dedicated

to my father, Marvin

and in memory of my mother, Selma

Acknowledgements

I would like to thank my academic advisor, Professor Lawrence Ruby of the department of Nuclear Engineering of the University of California. for all of his assistance and invaluable advice during the preparation of this thesis and during my tenure at the university. I would also like to thank my research supervisor, Professor Victor Perez-Mendez of the Lawrence Berkeley Laboratory. for his guidance while the research was being conducted as well as his help with the various drafts of the thesis.

I wish to thank Dr. Terrence A. Mulera of the Lawrence Berkeley Laboratory for his patience in answering my many questions and for his sense of humor. I acknowledge the gracious assistance of Dane Anderberg and his staff at the glass shop of LBL. Thanks are due to Ezio Carboni of the Istituto Nazionale di Fisica Nucleare, sezione di Pisa, Italy for the drawings.

Finally, I thank Professor Alberto Del Guerra of the Dipatimento di Fisica dell' Universitá di Pisa, Italy for his support , his guidance, and his friendship during the last four years.

Table of Contents

CHAPTER ONE - Introduction

Since their discovery by Roentgen in 1895, x-rays have been the most widely used method of medical imaging. Their attractiveness lies in the different attenuation coefficients of bone and surrounding tissue. This, together with the good resolution of radiographic film, provides high quality images of anatomical structure. In addition, certain objects can be imaged with the introduction of materials with high x-ray absorption, such as barium or iodine[1]. Recently, radiation detectors have replaced film as the imaging medium. This digitized information is, with the aid of computers, reconstructed into an image. This method of imaging is known as digital radiography.

One form of digital radiography that has gained widespread use is x-ray computed tomography (CT)[2-4]. In CT the goal is the reconstruction of the attenuation coefficient as a function of position in a plane, or slice, of an object. If the object is scanned from various angles enough information can be obtained to solve the two dimensional distribution of attenuation coefficients. Various reconstruction methods, including

Filtered Back Projection and Fast Fourier Transform techniques, can be used to create the image. A major advantage of this technique is its ability to image low contrast objects.

In recent years, positron emission tomography (PET) has shown its usefulness as an imaging modality[5]. Here the source of radiation is internal rather than external; therefore, one can follow the flow of a radioisotope, its concentration at various points, or its metabolism. The attraction of PET lies in the fact that the two photons of positron annihilation are emitted 180° apart; the line of the positron interaction can then be inferred. For the line location one can operate two detectors in coincidence, eliminating the need for collimation. This allows a lower source strength to be used (since typical collimator transmissions are 2.5×10^{-5}), giving a lower dose to the patient. Another attraction is the abundance of medically useful positron emitting isotopes, including (but not limited to) ^{11}C, ^{13}N, ^{15}O, ^{18}F, ^{68}Ga, and ^{82}Rb.

The concept of a PET system was developed in 1953 by Brownell and co-workers[6]; later other systems were developed[7-9] and are used for medical research. These cameras are generally crystal scintillator ring

tomographs using NaI(Tℓ) crystals[9]. More recently Bismuth Germanate (BGO)[10] and Cesium Fluoride[11] crystals have been used.

The advent of multiwire proportional chambers (MWPC) in physics research[12] has led to their use in medical physics applications[13]. They have the advantages of a high rate capability, good spatial resolution, and the coverage of a large area for a low cost. They would seem to lend themselves readily to a PET application.

However, a major problem in applying gas-filled MWPC's to positron tomography is the poor detection efficiency for the 511 keV annihilation gamma in any gas, including the high-Z Xenon. The solution to this problem requires the development of a gamma ray "converter" which can absorb the photons and eject either a photoelectron or a compton scattered electron, which would then be detected by the wire chamber. The photoelectric effect is the more desirable of the two processes, since the cross section is higher for the high photon energy and since energetic electrons are emitted. Therefore, a high-Z converter is desirable in order to enhance this effect (since $\sigma \propto Z^5$). The converter, however, cannot be too thick, since the emitted photo- or compton-electrons will travel only a short distance

before depositing all of their energy inside the converter. The effective region of a solid, homogeneous converter is a very thin layer. Alternatively, a thick converter with many holes into which the electrons can escape and interact in the gas-filled region may be used.

Both of these methods have been explored. Bateman and co-workers[14] have devised a system of multiple anodes interleaved with laminated metal cathode foils which serve as the converter. The cathodes are segmented and adjacent cathodes have their segmentation perpendicular to each other for position determination. A stack of twenty such sections (twenty-one cathodes with twenty wire planes) provides a reported efficiency of ~11% and a spatial resolution of ~6 mm (although they more recently[15] report an efficiency of 6.5%).

The high-density drift space converter has been investigated at the Lawrence Berkeley Laboratory by Perez-Mendez and collaborators. At first the converter took the form of corrugated bands of lead strips connected to form a honeycomb[16]. It was then decided to make converters with a more uniform drift field that could be provided by the creation of a resistive surface on tubes of lead glass[17]. The lead glass tubes are fused

together to form a matrix, then treated in a hydrogen atmosphere at elevated temperatures to form a conductive layer on the surface of the tubes. An electric potential applied at the ends of the tubes provides a drift field.

Jeavons and co-workers[18] have also applied the principle of the high-density drift space to the detection of the annihilation gammas. Here the γ-ray converters are constructed of thin lead sheets interleaved with thin sheets of fiberglass-reinforced epoxy resin. These sheets are glued together; subsequently, 0.8 mm holes are drilled. The layers are connected by a linearly resistive chain to produce a drift electric field. An efficiency of 8.5% for a 1 cm thick converter and a spatial resolution of 3.5 mm for a 1 mm line source are reported.

It has been the goal of this work to continue the development of lead-glass tube gamma converters, with a final aim of the construction of a high spatial resolution positron emission tomograph (HISPET). In the following chapter, I discuss the MWPC used, as well as the electronic read-out system. In chapter three I describe the construction of the converters. In chapter four I present the results of a study designed to improve the

image resolution of the tomograph. Finally, in chapter five I give the results of the converter measurements, along with the design performance of HISPET.

CHAPTER TWO - Experimental Apparatus

To measure the efficiency and time resolution of the converter we used a detection system consisting of a multiwire proportional chamber (MWPC) operated in coincidence with a NaI(Tℓ) crystal. In this chapter I discuss the construction of the chamber and the read-out electronics.

II.1 The MultiWire Proportional Chamber

The MWPC consisted of one anode and two cathode wire planes, each with an active area of 15 × 15 cm^2. The anode wires were stainless steel wires of 20 μm diameter, and spaced 3 mm apart. The cathodes also were stainless steel wires, of 100 μm diameter and 2 mm spacing. The cathode wires were coupled to a common bus bar through 220 kΩ resistors. The anode-cathode gap was 5 mm. The cathodes were arranged perpendicular to each other to allow for the acquisition of position information via fast delay lines (specific delay 8 ns/cm, Z_0 = 145 Ω)[19]. The standard gas filling was P_{30} (70% Ar - 30% CH_4). The wire planes were placed in an aluminum box, the lid of which was one-quarter inch thick. At the center of the lid was a 100 μm thick mylar window, which allowed the passage of

low energy x-rays such as the 5.9 keV x-ray of ^{55}Fe. The chamber could be pressurized up to three atmospheres absolute.

The converters tested were constructed of lead-glass tubes fused to form a honeycomb matrix; all had an active area of 5 × 5 cm^2. Thicknesses of the converters were 5, 10, or 20 mm. They were placed at the center of the chamber, beneath the wires, at a distance varying from 2 to 15 mm from the bottom cathode. Figure 1 is a diagram of the set-up for coincidence detection of the annihilation gammas from ^{68}Ga. The NaI crystal was aligned so that the solid angle subtended was the same as that subtended by the converter.

Some of the physical dimensions (e.g. anode-cathode gap, anode wire diameter) were changed for the operation of the chamber in a self quenching streamer mode. These measurements will be described in chapter four.

II.2 Electronic Read-out System

II.2.1 Pulse Shaping Electronics

A diagram of the electronics system for both the anode and NaI crystal is presented in figure 2. The anode signal was fed into a fast (1.5 ns rise time) 220× amplifier, the output of which was fed into a constant fraction discriminator to eliminate time jitter. The following two discriminators shaped the signal for use with the coincidence unit.

The NaI pulse was fed into a discriminator whose threshold was set so as to eliminate any signal due to gammas below the 511 keV annihilation peak. The signal was then delayed and shaped in order to provide the window for the coincidence measurement (described below). To measure accidental coincidences a delayed signal was taken from the second gate generator and delayed 2 μs. The resultant window was set at the same width as for the true coincidences.

II.2.2 Coincidence and Time Spectrum Electronics

In order to make a coincidence measurement between the MWPC and NaI detectors we have to consider that the annihilation gammas can

interact anywhere within the thickness of the converter. The electrons will then drift out of the converter and into the wire chamber. Therefore, a window which will accept an electron produced at the bottom of the converter, as well as one produced at the top, must be created. To accomplish this we used a coincidence unit which produced a TRUE output whenever the two inputs were true simultaneously (rather than a coincidence unit that is leading edge triggered, producing an output when the second input is recorded within a prescribed time after the first). The pulse from the NaI crystal was stretched to provide a window (100 - 400 ns wide depending on the thickness of the converter) during which time a coincidence would be registered if an anode pulse appeared. An updating switch in the coincidence unit prevented the counting of more than one coincidence for a given NaI pulse.

This method also allowed us to measure a time spectrum with which we could see the distribution of coincidence events. This would give us an idea of the effective thickness of the converter, since we know the drift velocity of the electrons. For this measurement we used a LeCroy Model 3001 qVt in t mode, using the NaI signal as the START pulse, and the output

of the coincidence unit as the STOP. To ensure that the timing window was correct we used the anode signal for the STOP pulse, and adjusted the timing of the system so that the peak due to the converter was centered in the coincidence window.

Figure 3 shows three typical time spectra: the top two use the anode pulse as the STOP, the bottom one the coincidence pulse. Figures 3a and 3c show the coincidence peak with voltage applied to the converter. Figure 3b shows that with no voltage applied; its peak is due to conversion at the surface of the converter. The peak to the left of the converter peak in figures 3a and 3b is probably due to conversion of the annihilation gammas within the aluminum lid of the chamber.

CHAPTER THREE - Lead Oxide Glass Tube Converters

III.1 Construction of Converters

The method used to build the converters was the same as that developed by Lum, et al[20]. The basic steps necessary were the cutting and fusing of lengths of glass tubes, developing a protective layer of silica on the surface of the resultant matrix, creating a conductive layer of lead on the surface of the glass beneath the silica layer, and, finally, putting a uniform conductive layer on the surface of the converters. The entire process to create roughly five 5 × 5 cm^2 one cm thick converters (including cutting of the glass) took about two weeks time.

III.1.1 Fusing of Glass Tubes

We began with ~150 cm lengths of lead glass tubing of 0.48 mm inner diameter and 0.60 mm outer diameter[21]. Table 1 shows the physical properties of the glass used. The tubes were cut to 7 cm lengths and stacked in a graphite mold (see figure 4). Since "sawing" the tubes would have resulted in severely damaging the ends of the tubes, they were cut in the following manner: up to one hundred tubes were laid in a single layer

flush at one end. Masking tape was placed on the rows of the tubes in seven centimeter spacings. The glass surface was then "nicked" with a carbide blade. Subsequently pressure was applied so that the fracture propagated around the tube resulting in a clean edge.

Enough tubes were cut so that there was approximately a 2 mm gap between the mold and its lid. This allowed for some settling of the tubes upon heating, as well as for compression of the tubes upon fusing.

TABLE I

Physical Properties of Nuclear Pacific Hi-D Glass

Composition by weight	79% PbO, 19% SiO_2, 1% Al_2O_3, small percentage of As
Density	6.2 g/cm^3
Softening point	445 °C
Annealing point	397 °C
Thermal expansion coefficient	94.7×10^{-7} /°C

The mold was placed in a furnace, and the temperature was raised slowly (100 °C/hr) until the oven temperature was about 40° below the softening point of the glass. It was then left overnight at this temperature to allow the contents of the oven to reach thermal equilibrium. The following morning the temperature was raised 10 °C/hr. When the softening point (defined as that temperature at which the glass begins to deform under its own weight) was reached the glass was allowed to tack firmly. When the lid of the mold had closed completely the desired compression had been achieved, and the glass was kept at this temperature for a short while longer to allow the top layers to tack as firmly as the lower layers. The oven door was then opened so that the temperature would drop roughly thirty degrees. This stopped the sagging process. The temperature of the oven was then lowered to allow the glass to anneal for eight hours.

The fused boule was sawed into wafers of desired thickness, polished with carborundum paper, and then thoroughly cleaned in acetone (to degrease) and low conductivity water.

III.1.2 Development of a Protective Silica Film

After the wafers were cut, polished, and cleaned, a thin film of silica (~100 nm) was produced on the surface of the tubes. This film served to physically protect the reduced lead beneath, and, more importantly, prevented water vapor from reaching the conductive layer.

This layer was developed by treating the glass in dilute (0.1 M) hydrochloric acid for a period of time depending on the diameter of the tubes. For the 0.48 mm inner diameter tubing we treated the glass for two minutes. The film, which is soft when first formed, was dried and hardened in an oven at 140 °C for eight hours.

After treatment the silca film was identifiable by the interference colors produced by the film. These colors are much more noticable after the glass is blackened in the hydrogen treatment.

III.1.3 The Hydrogen Reduction Treatment

After completion of the formation of the silica layer the glass was ready to be treated in the hydrogen furnace. This furnace consisted of a vacuum-tight stainless-steel cylinder approximately 40 cm long with a

15 cm inner diameter. The wafers were placed in the cylinder so that the flow of the gas would be along the axis of the tubes, thereby facilitating the removal of water vapor. The gas was preheated by means of coils wrapped around the chamber so that it would be at the desired temperature upon entering the cylinder. Figure 5 shows a diagram of the system.

The procedure for the treatment was as follows: once the tubes were mounted in the cylinder it was bolted tight and placed in the oven. Helium was then flowed through the chamber, at a rate of approximately 4 ml/s, while the furnace was raised to the desired temperature. When the furnace reached this temperature the chamber (and the glass inside) was allowed to reach thermal equilibrium with the furnace overnight. The next morning hydrogen was admitted into the chamber at a rate of 15 ml/s, first passing through a dessicator and a particle filter. At the conclusion of the hydrogen treatment helium was reintroduced into the chamber as the temperature was brought down.

This hydrogen treatment reduces the lead oxide by the reversible reaction $PbO + H_2 \rightleftarrows Pb + H_2O$. It has been postulated[22] that the conductive layer produced is actually a semiconductive layer. It is possible

to tailor the surface resistivity developed on the glass by changing the temperature and the duration of the treatment. Figure 6 is a plot of the surface resistivity vs. temperature of treatment. All of these treatments were performed for six hours. Blodgett[22] has shown that as the temperature of the treatment rises this curve passes through a minimum and the final resistivity produced will rise with increasing temperature. We have chosen not to experiment at higher temperatures for fear of approaching the softening point of the glass, thus ruining the converters.

As can be seen from the figure, for higher values of resistivity the curve is very steep and a difference of three orders of magnitude can be obtained by varying the temperature less than thirty degrees! This made it very difficult to produce a desired resistance in that region. We have briefly experimented with altering the treatment time at a constant temperature by extrapolating Blodgett's data (for 60% PbO glass) to our data for 80% PbO glass. The results showed that after three hours the resistivity was the same as that produced over six hours. This suggests that the glass with the higher lead content approaches its asymptotic value for the resistivity more quickly.

It is also important to have the resistance produced within a certain range. Too low a value for the resistivity would result in a greater dissipation of power in the converter ($P=V^2/R$) and the resulting heat could damage the converter. On the other hand, too high a value for the resistivity would result in a DC current along the tube walls insufficient to effectively remove charges which build up on the walls. Figure 7 is an estimate of the percentage of the DC current as a function of count rate and surface resistivity. In calculating these figures "worst case" assumptions were used throughout. For example, we have calculated[28] an average of 15 ion pairs created per event. However, we have estimated that as many as 200 ion pairs can be created per event. This number was used. Also I have assumed that every charge created will attach to the tube wall (this is truly worst case. If it were so, no electrons would reach the MWPC and the converter would not work!). For our expected count rate of 375 kHz per module, a surface resistivity of up to 10^{17} Ω/sq would be acceptable.

III.1.4 Formation of a Uniform Conductive Surface on the Converters

Once a uniform resistive layer has been created on the surface of the converter tubes, it is necessary to have the ends of each tube at the same potential. This will ensure that the same electric field is present in each tube of the converter. To accomplish this we need to coat each surface of the converter with a highly conductive material, so that there will be minimal resistance on the surfaces of the converter.

In previous work in the development of lead-glass tube converters[17], conductive silver epoxy was applied to the tubes. For tubes of diameter larger than those of this work this was a convenient solution. However, there were difficulties which precluded the use of silver epoxy with the 0.48 mm ID tubes.

The epoxy had been applied by dabbing the surface with a rubber stopper. This method, rather than brushing or rolling, was employed in order to avoid clogging the tubes with epoxy. While this method was successful with the larger diameter tubes, we found that it was not possible to avoid clogging a small percentage of the smaller tubes.

A second problem with the epoxy was that it was difficult, if not impossible, to apply the coat uniformly. This gave rise to irregularities in the electric field inside the converter tubes, impairing the efficiency of the converter. A further problem caused by non-uniformity was that of arcing along the surface of the converter. This had the unfortunate effect, in one case, of actually melting the converter!

To solve this problem it was decided to plate the surface of the converter with a metal in a vacuum deposition tank. The metal was vapor plated at an angle 80° normal to the surface of the converter. This would ensure good adhesion of the metal to the glass and that there would be little metal plated inside the tube. For 0.48 mm ID tubes metal was plated 80 μm inside the tube.

The first metal tried was copper. We were able to create a uniformly conductive surface – the average resistance along the surface was 50 Ω. However, when there was arcing to the surface of the converter from the cathode, the copper apparently vaporized, leaving non-conductive spots on the converter. We finally settled on molybdenum, which has a much higher boiling point than copper (4612 °C vs. 2567 °C) and a reasonable electrical

resistivity (5.2 μΩ/cm vs. 1.67 μΩ/cm). Best results were obtained with the molybdenum plating.

III.2 Lateral Diffusion of Electrons Within Converter Tubes

III.2.1 Brief Discussion of Electron Diffusion in Gases

Electrons which drift along the electric field within the converter exhibit a transverse diffusion which can be given[23] by a Gaussian of the form

$$\frac{dN}{N} = \frac{1}{\sqrt{4\pi Dt}} e^{-(x^2/4Dt)} dx \qquad (1)$$

where dN/N is the fraction of charge in an element dx at a distance x from the origin after a time t. D is the diffusion coefficient, and can be written as

$$D = \frac{v\ell}{3} \qquad (2)$$

where ℓ is the mean free path of the drift electrons, and v is the instantaneous velocity of the electrons[24].

The distribution of equation (1) has a standard deviation

$$\sigma_x = \sqrt{2Dt} \qquad (3)$$

The drift time, t, can be represented by x/w, where w is the drift velocity (different than the instantaneous velocity, v) of the electrons in the gas. σ_x then becomes

$$\sigma_x = \sqrt{\frac{2Dx}{w}} \qquad (4)$$

A characteristic energy, ϵ_K, of the gas can be defined[25] as

$$\epsilon_K = \frac{\varepsilon DE}{w} \qquad (5)$$

Inserting this into equation (4) yields

$$\sigma_x = \sqrt{\frac{2\epsilon_K x}{\varepsilon E}} \qquad (6)$$

which can be amended to show the following:

$$\sigma_x = \sqrt{\frac{2\epsilon_K}{\varepsilon \frac{E}{P}} \frac{x}{P}} \qquad (7)$$

This equation has very important consequences. First, it is easily seen that, for a given value of E/P, the transverse diffusion of the

electrons will decrease with an increase in pressure. Second, we see that the diffusion is dependent on the electric field present.

This field dependence, however, is a bit more subtle than it first appears. It would seem that one could increase the drift field indefinitely, continuously decreasing the standard deviation of the distribution. However, the dependence of ϵ_K on the drift field, E, gives us, in fact, an electric field at which there is a minimum in the σ_x (see, for example, figure 8 of reference 25). The drift field inside the converter must be adjusted to give this minimum diffusion. We have experimentally determined this drift field to be ~400 V/cm at 1 atm pressure[26].

III.2.2 Loss of Expected Efficiency in Thick Converters

While experimenting with converters of various thicknesses we noted that the measured efficiencies of one and two cm thick converters did not agree with those predicted by Monte Carlo calculations[27], although a 5 mm thick converter did produce the expected efficiency (see table 2). In addition, the time spectra for the thick converters were narrower than expected. This indicated to us that electrons were being drawn from less

TABLE 2

Time Spectrum and Efficiency for 0.48 mm ID Tubing Converter

(P_{30} at 2 atm, E/P = 400 V cm^{-1} atm^{-1})

Converter Thickness (cm)	Experimental Time Spectrum FWHM (ns)	Experimental Efficiency (%)	Monte Carlo Efficiency*
0.5	60 ± 10	3.5 ± 0.25	3.56 ± 0.11
1.0	90 ± 10	5.8 ± 0.22	6.40 ± 0.15
2.0	95 ± 10	6.8 ± 0.25	11.71 ± 0.27

* mean and standard deviation of the mean of five runs (3000 cases each) [from ref. 27]

than the full thickness of the converters. The time spectra for the three converters are shown in figure 8. Note that the shape is roughly Gaussian. We would expect a uniform distribution because electrons are produced more or less uniformly throughout the converter.

At first we attributed the problem to having converters with too high a resistance. The drop in efficiency, we believed, was due to charging up of the walls of the tubes and the resultant distortion of the electric field. This theory, however, was discarded when the effect was seen with converters of lower resistivity. We began to research the

possibility that diffusion of the electrons was the cause of our problem. Figure 9 is taken from reference 24 and is a graph of transverse diffusion as a function of the reduced electric field. From this figure we assume that at our field (400 V/cm/atm) the standard deviation of the dispersion is 1600 μm for our gas mixture (P_{30}). This data, however, is taken at 600 torr for a 15 cm drift length. Correcting to our conditions of 2 atm and 1 cm drift (using equation 7) we find that $\sigma_x \approx 260$ μm. Since the inner radius of our tubes is 240 μm, it seems that our problem was, in fact, caused by diffusion of the electrons into the walls of the glass.

III.2.3 Solution of the Problem

Given equation 7 we decided that increasing the pressure of the chamber to 3 atm would be the best way to solve the problem. Increasing the pressure by a factor of 1.5 reduces the dispersion by a factor of 1.22 to 210 μm. The time spectra for the one cm thick converter at three atm is shown in figure 10. Note that the spectrum is now much flatter, indicating that we are drifting electrons throughout the length of the converter. The efficiency of the converter at three atm was 6.65%, agreeing with the predictions of reference 27.

CHAPTER FOUR– Self Quenching Streamers

As early as 1968 it was seen[29] that wire chambers could be operated somewhat beyond the proportional region, without reaching the Geiger-Müller region. This effect manifested itself in large pulses (smaller than Geiger pulses), the amplitudes of which were almost independent of the primary ionization deposited in the chamber. These large pulses were seen again a few years later[30] in multiwire chambers. Here it is noted that the pulses seem to be dependent upon the thickness of the anode wires: the effect is more pronounced with thicker wires. It is also reported that there is a very short dead time associated with these pulses, unlike those of Geiger-Müller discharge. More recently this effect has been studied in greater depth[31-35] ; this mode of chamber operation has come to be known as the Self Quenching Streamer mode.

IV.1 Some Considerations on Self Quenching Streamers

The self quenching streamer (SQS) is characterized by the fact that the amount of charge collected at the anode is independent of the amount of energy deposited in the chamber by the incident particle. This is shown

clearly in figure four of reference 32, in which the charge produced by β^- particles (^{90}Sr) is compared with that produced by 5.9 keV x-rays (^{55}Fe). The avalanche is saturated in this sense, although the pulse height does rise with applied voltage. Moreover, the charge collected in SQS mode is up to two orders of magnitude greater than that collected in the proportional mode of operation[32].

Other characteristics of these pulses include their very fast rise time, short duration, and quick fall time (although this does seem to be a function of the amount of quenching gas used[34]). These pulses also produce a dead time much shorter than that produced in GM operation and the "dead zone" does not spread along the entire length of the wire (as in GM); rather, it is confined to distances ranging from a few mm to a few cm, depending on the gas composition.

This saturation would appear to be a space charge effect. However, the saturation of space charge does not propagate along the wire. Photographic evidence in references 32 and 33 shows clearly that the avalanche propagates outward, orthogonal to the anode wire. In the

photographs it is clearly seen that the streamer propagates away from the anode and in the direction of the original avalanche.

A possible explanation of the mechanism of streamer formation follows: the high electric field at the anode wire produces a high multiplication of electrons, and an equivalent number of positive ions. These positive ions, drifting away from the anode, form, together with the ionization electrons, a dipole field which is superimposed on the field of the anode wire (see figure 11). Photons produced by radiative recombination ionize other gas molecules, and those electrons produced in the vicinity of the dipole field accelerate towards the positive end of the dipole. The positive ions continue to drift away from the anode and this process continues until the dipole dies away and can no longer support the formation of an avalanche.

What advantages does this mode of chamber operation offer us for positron emission tomography? The fact that the pulses do not have so great an amplitude range as do proportional pulses allows us to simplify the amplification electronics (and allows us to use leading edge discriminators). The large anode wires necessary for the formation of the

streamers enables us to construct sturdier chambers. Most importantly, the direction of streamer formation perpendicular to the anode wire gives us information as to the origin of the event. In a planar positron camera in which the MWPC is sandwiched by two converter planes we can deduce, from the relative amplitude of the signals induced on the two cathodes, in which converter the interaction took place. This will have the effect of greatly reducing the parallax error in image reconstruction and, therefore, will improve the image resolution of the camera.

IV.2 Experimental Set-up for SQS Measurements

With this in mind we set out to discover if we could, indeed, discriminate the half of the chamber in which the interaction took place, and, if so, whether this discrimination agreed with our knowledge of where the interaction actually took place. We first tried to see the difference qualitatively using an oscilloscope. Later we attempted to quantify this difference. We used the following sources: ^{55}Fe, whose 5.9 keV x-ray should interact in the top half-gap of the chamber; ^{90}Sr, whose β^- particles should deposit energy throughout the chamber, leaving virtually no top-

bottom difference; ^{68}Ga, a β^+ emitter, whose 511 keV annihilation gamma ray should interact in the converter at the bottom of the chamber.

IV.2.1 Chamber Configuration

To ensure that we could discriminate events in the top or bottom half-gap of the chamber we first needed to see that our chamber could, in fact, be operated in SQS mode. With the chamber configuration described in chapter two some large amplitude pulses were seen before the onset of continuous discharge but this appeared to be a mixture of the proportional and SQS regimes. It was postulated that because of the small anode-cathode gap (5 mm), the streamer propagated outward to the cathode, resulting in a discharge. By inserting spacers between the wire planes we increased the anode-cathode gap to 10 and 15 mm. However, we were not able to operate exclusively in the SQS regime with the 20 μm anode wires, even with different gas mixtures at up to two atmospheres of pressure.

We then built a plane of 75 μm diameter copper-berylium wires with a wire spacing of 2 mm. Here, using argon with various quenching gases (CH_4, C_2H_6, C_4H_{10}) no streamers were seen. Here we postulated that the

wire spacing was too small for streamer formation. The high voltage needed to obtain the requisite electric field caused static discharges. By removing every other wire we increased the spacing to 4 mm. Here we were able to observe SQS pulses with various gas mixtures and anode-cathode gaps. The conditions in which we were able to observe the SQS regime are summarized in table 3.

Satisfied that we were able to produce the self quenching streamer regime we set out to study the differences in the pulses induced on each cathode plane. To do this we needed to collect and measure these signals. The delay lines were replaced by copper foils capacitively coupled to the cathodes in the same manner as were the delay lines. The signal was read through a coupling capacitor (terminated in 10 kΩ – 1 MΩ) then through a high impedance probe to a Tektronix model 454 oscilloscpe. The signal from the top cathode was fed into channel 1 of the scope; that of the bottom cathode was fed into channel 2. For greater ease in comparison the bottom signal was inverted. The two signals could then be viewed either in "alternate" mode on the scope, or in "add" mode, in which the two signals

TABLE 3

Summary of SQS Regime with 4 mm Anode Wire Spacing

Gas Mixture	Anode-Cathode Gap (mm):	5.0		10.0		15.0	
	Gas Pressure (atm):	1.2	2.0	1.2	2.0	1.2	2.0
Ar/CH_4	70/30			P	P S		
	50/50	P	P S	P	P S	P	P S
	30/70			P	P S		
Ar/C_2H_6	70/30			P	P S		
	50/50	P S	P S	P S	P S	P S	P S
	30/70			P S	P S		
Ar/Co_2	70/30			P	P S		
	50/50	P S	S	P S	S	P S	P S
	30/70			S	S		
Ne/CO_2	70/30			P	P S		
	50/50	P S	P S	P S	P S	P	P S
	30/70			P S	P S		

P = proportional regime
S = self quenching streamer regime

are summed with the resultant signal appearing on the scope. By adding the pulses together the sum would tell us in which direction the streamer had propagated, thus telling us in which half-gap of the chamber the interaction took place. Figures 12 through 14 show the alternate and added signals for, respectively, ^{55}Fe, ^{90}Sr, and ^{68}Ga. From these photographs it is clear

that the majority of ^{55}Fe interactions occured in the top half-gap of the chamber, and that the majority of ^{68}Ga interactions occured in the bottom half-gap. This distinction cannot be made for the ^{90}Sr pulses. However, these results qualitatively confirm our expectations about the location of the events. The next step was to quantitatively confirm them.

IV.2.2 Electronics for Quantitative Top-Bottom Discrimination

A diagram of the electronics set-up for the quantitative discrimination of events occuring in either the top or bottom half-gap is presented in figure 15. The signals from the two cathodes were fed into a 72× difference amplifier, the output of which was fed into a linear gate/pulse stretcher. This linear gate/pulse stretcher produced both a NIM standard output, which was fed into a scaler, and an analog signal, which was fed into a LeCroy Model 3001 qVt (in V mode) to look at the pulse height distributions.

It was the difference amplifier which allowed us to compare the amplitudes of the pulses from the two cathodes. Figure 16 is a schematic diagram of this amplifier, which functions as follows: the signals from

the two inputs are subtracted (BOTTOM from TOP). If the result is positive it is amplified approximately 72× and fed out. If, on the other hand, the result is negative, a 75 mV negative pulse is output. This negative pulse gave us some problems in that the overshot of the pulse was counted as a small positive pulse. This problem was alleviated by gating the linear gate with the anode signal; the gate was wide enough to accept only the true signal.

The coincidence system with the NaI detector was added only when we studied the ^{68}Ga source. Here we vetoed the linear gate in the absence of a coincidence between the anode and the NaI. The signal from the NaI detector was fed into the veto input of the coincidence unit so that only a coincidence would produce a zero input which would unblock the linear gate.

With this set-up we found that with a ^{55}Fe source 89% of the interactions took place in the top half-gap of the chamber, agreeing with the calculated value of 85% (see Appendix A) obtained by using cross sections by Hubble[36]. The pulse height distribution for ^{55}Fe is shown in

figure 17. For ^{90}Sr we found approximately 55% of the events occuring in the top half-gap.

In taking measurements with ^{68}Ga we needed to take into account conversionof the gammas in the aluminum lid of the chamber as well as at the surface of the converter. We therefore needed to subtract the converter voltage ON measurements from those taken with the converter off in order to see the contribution of the converter itself. The results are shown in table 4.

TABLE 4

Top-Bottom Cathode Discrimination for 511 keV γ-rays

	Converter Voltage ON	Converter Voltage OFF	Net Contribution due to the Converter
Absolute Efficiency	4.6×10^{-2}	0.5×10^{-2}	4.1×10^{-2}
Relative Contribution			
Bottom > Top	88%	61%	91%
Top > Bottom	10%	11%	9%
|Bottom - Top| < Noise	2%	28%	-

It is easily seen from the above that operation in the SQS regime will enable us to determine to a good degree of accuracy the location of an

event in either half of the chamber, thereby reducing the parallax error in image reconstruction. In the proposed positron camera we expect to be able to discern this difference with a 90% level of confidence, reducing the parallax error by a factor of three[27].

CHAPTER FIVE - Conclusion

Measurements were made on converters cut to three different thicknesses: 5, 10, and 20 mm. The five mm piece was coated with silver epoxy to produce the conductive surface for application of the drift field; the other pieces were plated with molybdenum. Table 2 (page 24) shows measurements of efficiency and time resolution for each converter at two atmospheres of pressure. In addition, Monte Carlo calculated efficiencies are presented for each converter[27]. As has been described in chapter three, we were able to regain the expected efficiency for the 10 mm converter, measuring 6.65% ± 0.04, by increasing the pressure to three atmospheres. The measured time resolution was 160 ns FWHM. These results are roughly a factor of 1.5 better than the efficiency measured for a 10 mm thick converter made of tubes of 0.90 mm inner diameter [26].

The data obtained from these measurements has led us to the design of a High Spatial resolution Positron Emission Tomograph (HISPET). As proposed, HISPET will consist of six modules arranged to form the lateral surface of a hexagonal prism. Each module will contain two MWPC's, each sandwiched by two 1 cm thick converter planes (see figure 18). Owing to

absorption in each converter the true efficiency for one module will be 22.5%.

It can be shown (see, for example, reference 37) that for a given ratio of true to accidental coincidences (T/A = constant), the coincidence rate T for a tomograph can be given as

$$T = \frac{1}{2\frac{T}{A}} \cdot \frac{\eta^2}{\tau} \qquad (6)$$

where η is the efficiency of one module, τ is the time resolution of one module. For HISPET, with a true to accidental ratio of 3:1, this gives us a coincidence rate of 84 kHz. Data for the tomograph will be reconstructed using limited angle algorithms[38]. Characteristics and expected performance of the tomograph are given in table 5.

TABLE 5

Characteristics and Performance of HISPET

Number of Modules	6
Characteristics of each module:	
Number of MWPC	2
Number of layers of converter for each MWPC	2
Active area of the first layer	45 × 45 cm^2
Converter tube diameter	0.48 mm
Total converter thickness	4 × 1 cm
Gas pressure	2 - 3 atm
Efficiency for 511 keV γ-rays	22.5%
Covered solid angle	2π
Performance of the tomograph in air:	
Coincidence efficiency for β^+ decay	2.2%
Coincidence resolving time	100 ns
EGS calculated intrinsic spatial resolution (^{18}F source)	≤ 4.5 mm (FWHM)
True coincidence to accidental coincidence ratio T:A	3 : 1
Source strength	~300 μCi
Single rate per module	375 kHz
True coincidence rate per module pair	84 kHz
True coincidence rate for the tomograph	252 kHz
Total coincidence rate (T + A) for the tomograph	336 kHz

Performance of the tomograph for a uniform activity in a cylindrical water phantom (~10 cm long × 10 cm radius):

Volume sensitivity (for T/A = 3)	100000 c/s per 0.1 μCi/ml
Statistical uncertainty of the signal per voxel (accidental coincidences subtracted):	
- 6 × 6 × 10 mm^3 voxel in 1 min	~7%
- 2 × 2 × 10 mm^3 voxel in 5 min	~10%
EGS calculated Compton distributed noise	~1/3

APPENDIX A

Calculation of Location of ^{55}Fe X-ray Interaction in the Wire Chamber

In order to calculate the percentage of events occuring in either half-gap of the chamber we need to know the distances involved and the proper attenuation coefficient. Essentially, the situation can be depicted in figure 19. Letting N_0 equal the input flux and N_1 equal the flux crossing the anode plane, we see easily that

$$N_1 = N_0 e^{-\mu d_1} \tag{9}$$

Therefore, the number of interactions in region 1,

$$N_{int\ 1} = N_0 - N_1 = N_0 \left(1 - e^{-\mu d_1}\right) \tag{10}$$

Similarly, the number of interactions in region 2,

$$N_{int\ 2} = N_1 \left(1 - e^{-\mu d_2}\right)$$

$$= N_0 e^{-\mu d_1} \left(1 - e^{-\mu d_2}\right) \tag{11}$$

The ratio of interactions, R, is therefore given by

$$R = \frac{N_{int\ 1}}{N_{int\ 2}} = \frac{N_0\left(1 - e^{-\mu d_1}\right)}{N_0\ e^{-\mu d_1}\left(1 - e^{-\mu d_2}\right)}$$

$$R = \frac{e^{\mu d_1}\left(1 - e^{-\mu d_1}\right)}{\left(1 - e^{-\mu d_2}\right)} \qquad (12)$$

Here it is necessary only to calculate the mass attenuation coefficient, μ, for our 70% Ar – 30% CH_4 gas mixture at two atmospheres of pressure. Since the coefficient is generally given in units of μ/ρ (cm^2/g), we need to know the density of the gas. Using the ideal gas law, $PV = nRT$, we find that $\rho = n/V = 8.31924 \times 10^{-5}$ moles/cm^3 (given 2 atm, 20 °C).

To calculate μ we note that for a gas mixture we have a weighted expression

$$\mu_{mixture} = \sum_i w_i \left(\frac{\mu}{\rho}\right)_i \rho_i \qquad (13)$$

where w_i is the proportion by weight of each i^{th} element.

Table 6 gives the weights, as well as the interpolated μ/ρ values, for each element in the gas. The calculated value for the attenuation coefficient, $\mu = 7.525 \times 10^{-1}$. Using this result, and inserting it along with

the distances given in figure 19 gives us a ratio of interaction R = 5.582. That is, 85% of the interactions should occur in the top half of the chamber, 15% in the bottom half.

TABLE 6

Proportion by Weight and Attenuation Coefficient for P_{30} Gas

Element	w_i	μ/ρ (cm^2/g)
Ar	0.8531	265.0
C	0.1100	10.94
H	0.0369	0.02131

APPENDIX B

Measurements on Lead Glass During LBL-Pisa Collaboration

As part of the collaboration between the Lawrence Berkeley Laboratory and the University of Pisa, I have spent the calendar year 1984 in Italy continuing the development of HISPET. In this appendix I describe the work done during that year.

The most important development during this year was our decision to change the type of lead glass used for the converters. Figure 20 is a graph of Monte Carlo calculated efficiency of a 1 cm thick converter vs. tube outer diameter for a constant ratio of outer to inner diameter tubes[39]. Curves are drawn for lead-glass tubes containing the indicated percentage of PbO. The percentages used are those of commercially available glass that we have used. The curve for solid lead is shown for comparison. Notice that there is only a very slight loss of efficiency going from the 79% PbO glass to the 71% PbO glass. This is probably due to a balancing of a loss of gamma absorption in the lower lead content glass with a gain of electron range (that is, a greater probability of detection of the Compton - or photo - electron) in the lower lead content glass.

This 71% PbO glass offers us a distinct advantage over the 79% PbO glass: it is much easier to draw into tubes. When being drawn into tubes the 79% PbO glass has a tendency to devitrify, making it very difficult to work with, as well as causing much waste during the drawing process. The 71% PbO glass does not divitrify so readily. It is therefore easier, and, more importantly, much less expensive to draw into the very small tubes required for our converters.

Given the nearly equal efficiency expected for the two glasses, we decided to switch to the 71% PbO glass. This glass is made by Schott; its physical properties are presented below.

TABLE 7

Physical Properties of Schott RS-520 Glass

PbO content	71% by weight
Density	5.18 g/cm^3
Softening point	538 °C
Annealing point	423 °C
Thermal expansion coefficient	81×10^{-7} /°C

This Schott glass was extensively studied. The resistance produced during the hydrogen treatment was examined as a function of both temperature and time. Figure 21 is a graph of resistance vs. temperature for one 10 cm tube (5 mm ID/7 mm OD) for a six hour treatment. The minimum was found to occur at 360 °C. Figure 22 is a graph of resistance vs. time of the treatment for a single tube; all treatments were performed at 360 °C. Note that the value of the minimum resistance for the 71% PbO glass is nearly 2 orders of magnitude higher than that of the 79% PbO glass (figure 6); in addition, it is higher than that of the 60% PbO glass reported by Blodgett[22]. This could be due to several things: the system used in Italy was very different than that used at LBL (see reference 40 for a detailed description of the system used at the national laboratories at Frascati, Italy), although it is unlikely that this contributed greatly. More likely, the discrepancy was caused by the poor contacts with which we measured the resistivity. Some converters produced in Frascati showed a difference of two orders of magnitude after being plated with nickel[40].

REFERENCES

1. Parker, R.P., Nucl. Inst. and Meth. in Phys. Res., 221, 1984, 221.

2. Boyd, D.P., IEEE Trans. Nucl. Sci., NS-26, 1979, 2836.

3. Hounsfield, G.N., Brit. J. Radiol., 46, 1973, 1016.

4. Cormack, A.M., Phys. Med. Biol., 18, 1973, 195.

5. Brownell, G.L., Budinger, T.F., Lauterbur, P.C., McGeer, P.L., Science, 215, 1982, 619.

6. Brownell, G.L., Sweet, W.H., Nucleonics, 11, 1953, 40.

7. Tompson, C.J., Yamamoto, Y.L., Meyer, E., Proc. Soc. Photo-Opt. Instrum. Eng., 96, 1976, 263.

8. Cho, Z.H., Chan, J.K., Eriksson, L., IEEE Trans. Nucl. Sci., NS-23, 1976, 613.

9. Derenzo, S.E., Budinger, T.F., Cahoon, J.L., Greenberg, W.L., Huesman, R.H., Vuletich, T., IEEE Trans. Nucl. Sci., NS-26, 1979, 2790.

10. Hoffman, E., Phelps, M., Huang, S., Plummer, D., Kuhl, D., IEEE Trans. Nucl. Sci., NS-29, 1982, 469.

11. Allemand, R., Gresset, C., Vacher, J., J. Nuc. Med., 21, 1980, 153.

12. Charpak, G., Bouclier, R., Bressani, T., Favier, J., Zupancic, C., Nucl. Inst. and Meth., 62, 1968, 262.

13. Perez-Mendez, V., IEEE Trans. Nucl. Sci., NS-23, 1976, 1334.

14. Bateman, J.E., Connolly, J.F., Stephenson, R., Flesher, A.C., Nucl. Inst. and Meth., 176, 1980, 83.

15. Bateman, J.E., Connolly, J.F., Stephenson, R., Flesher, A.C., Nucl. Inst. and Meth., 217, 1983, 77.

16. Chu, D., Tam, K.C., Perez-Mendez, V., Lim, C.B., Lambert, D., Kaplan, S.N., IEEE Trans. Nucl. Sci., NS-23, 1976, 634.

17. Lum, G.K., Green, M.I., Perez-Mendez, V., Tam, K.C., IEEE Trans. Nucl. Sci., NS-27, 1980, 157.

18. Jeavons, A., Kull, K., Lindberg, B., Lee, G., Townsend, D., Frey, P., Donath, A., Nucl. Inst. and Meth., 176, 1980, 89.

19. Lecomte, P., Perez-Mendez, V., Stoker, G., Nucl. Inst. and Meth., 153, 1978, 543.

20. Lum, G.K., Anderberg, D., Green, M.I., Henrikson, P., Perez-Mendez, V., Proc. 25th Amer. Soc. Glassblowers Symp., Albany, N.Y., June 25 - 27, 1980.

21. Tubes drawn by Garner Glass Co., 177 S. Indian Hill Road, Claremont, CA 97111.

22. Blodgett, K.B., J. Amer. Cer. Soc., 34, 1951, 14.

23. Sauli, F., CERN 77-09, 1977.

24. Nygren, D., PEP-198, in 1975 PEP Summer Study Proceedings, LBL-4800, 1975.

25. Palladino, V., Sadoulet, B., Nucl. Inst. and Meth., 128, 1975, 323.

26. Del Guerra, A., Perez-Mendez, V., Schwartz, G., Sleaford, B., International Conference on Applications of Physics to Medicine and Biology, Alberi, G., Bajzer, Z., Baxa, P. eds. (World Scientific Publishing Co., 1982, Singapore) 355.

27. Del Guerra, A., Perez-Mendez, V., Schwartz, G., Nelson, W.R., IEEE Trans. Nucl. Sci., NS-30, 1983, 646.

28. Bellazzini, R., Del Guerra, A., Massai, M., Nelson, W.R., Perez-Mendez, V., Schwartz, G., IEEE Trans. Nucl. Sci., NS-31, 1984, 645.

29. Campion, P.J., Int. J. Appl. Rad. Isotopes, 19, 1968, 219.

30. Charpak, G., Rohm, D., Steiner, H., Nucl. Inst. and Meth., 80, 1970, 13.

31. Brehin, S., Diamant Berger, A., Marel, G., Tarte, G., Turlay, R., Charpak, G., Sauli, F., Nucl. Inst. and Meth., 123, 1975, 225.

32. Alekseev, G.D., Kalinina, N.A., Karpukhin, V.V., Khazins, D.M., Kruglov, V.V., Nucl. Inst. and Meth., 177, 1980, 385.

33. Atac, M., Tollestrup, A.V., Potter, D., Nucl. Inst. and Meth., 200, 1982, 345.

34. Mulera, T., Perez-Mendez, V., Nucl. Inst. and Meth., 203, 1982, 609.

35. Battistoni, G., Iarocci, E., Nicoletti, G., Trasatti, L., Nucl. Inst. and Meth., 152, 1978, 423.

36. Hubbel, J.H., Rad. Res., 70, 1977, 55.

37. Jeavons, A.P., Townsend, D.W., Ford, N.L., Kull, K., Manuel, A., Fischer, O., Peter, M., IEEE Trans. Nucl. Sci., NS-25, 1978, 164.

38. Tam, K.C., Perez-Mendez, V., J. Opt. Soc. Am., 71, 1981, 582.

39. Del Guerra, A., Conti, M., Nelson, W.R., proceedings of the "VII International Conference on Positron Annihilation", New Delhi, India, January 6-11, 1985, to be published.

40. Schwartz, G., Cinti, M., Conti, M., Del Guerra, A., Di Fino, M., Habel, R., Righini, L., ENEA internal report, 1985, to be published.

Figure Captions

1. Diagram of experimental set-up for coincidence detection of annihilation gammas from ^{68}Ga (not to scale).
2. Schematic diagram of read-out system for coincidence electronics.
3. Typical time spectra for ^{68}Ga source. All use the NaI signal as the START pulse. a) anode STOP, converter ON. b) anode STOP, converter OFF. c) coincidence STOP, converter ON. The peak at the left in a) and b) is probably due to gamma conversion in the aluminum lid of the chamber.
4. Diagram of glass tubes stacked in graphite mold.
5. Schematic diagram of hydrogen treatment system (from ref 20).
6. Resistivity in ohms/square of 80% PbO glass vs. temperature of hydrogen reduction treatment. All were performed for six hours. Data for 60% PbO glass are taken from reference 22.
7. Flux of ions attaching to tube walls as percentage of DC current along tubes at 1000 V/cm vs. resistivity of glass. Proposed count rate for HISPET is 375 kHz.

8. Time spectra for 5, 10, and 20 mm converters, respectively, at two atmospheres of pressure. The FWHM of each is given in table 2.

9. Transverse diffusion of drift electrons in Argon/CO_2 and several Argon/CH_4 mixtures as a function of E/P. For our gas mixture (70% Ar – 30% CH_4) we would expect σ = 1600 μm for 15 cm drift at 600 torr (from reference 24).

10. Time spectrum of 10 mm converter at 3 atmospheres pressure. FWHM = 160 ns.

11. Propagation of a self quenched streamer pulse. The strong dipole field attracts electrons that are produced by recombination photons. This field grows intil it can no longer support the avalanche process, and the electrons are collected at the anode.

12. Alternate and added signals for ^{55}Fe x-rays. The positive signal comes from the top cathode; the negative signal from the bottom cathode. It is clearly seen that most of the large amplitude pulses are at the top cathode.

13. Alternate and added signals for a ^{90}Sr source. Here it is difficult to differentiate the top and bottom cathodes.

14. Alternate and added signals for a ^{68}Ga source. Here most of the interactions appear to occur in the bottom half of the chamber.

15. Schematic diagram of read-out electronics for SQS top/bottom discrimination. The NaI signal is used only for ^{68}Ga testing.

16. Schematic diagram of 70× MWPC amplifier.

17. Pulse height spectrum showing the difference between the top and bottom cathodes, with a ^{55}Fe source. The bottom>top part of the spectrum has been inverted for the figure.

18. Schematic drawing of the hexagonal tomograph.

19. Diagram of physical dimensions of the MWPC.

20. Calculated Monte Carlo efficiency of 1 cm thick converters vs. outer diameter of lead-glass tubes, for a constant ratio of outer to inner diameter. Curves are drawn for lead-glass tubes containing the indicated percentage of PbO. These percentages are those of commercially available glass that we have used. The curve for solid lead is shown for comparison.

21. Graph of resistance vs. temperature (in ohms/tube) for a single 10 cm tube (5mm/7mm ID/OD) of 71% PbO Schott RS-520 glass. All treatments were performed for 6 hours.

22. Graph of resistance vs. time of treatment (in ohms/tube) for a single 10 cm tube (5mm/7mm ID/OD) of 71% PbO Schott RS-520 glass. All treatments were performed at 360 °C.

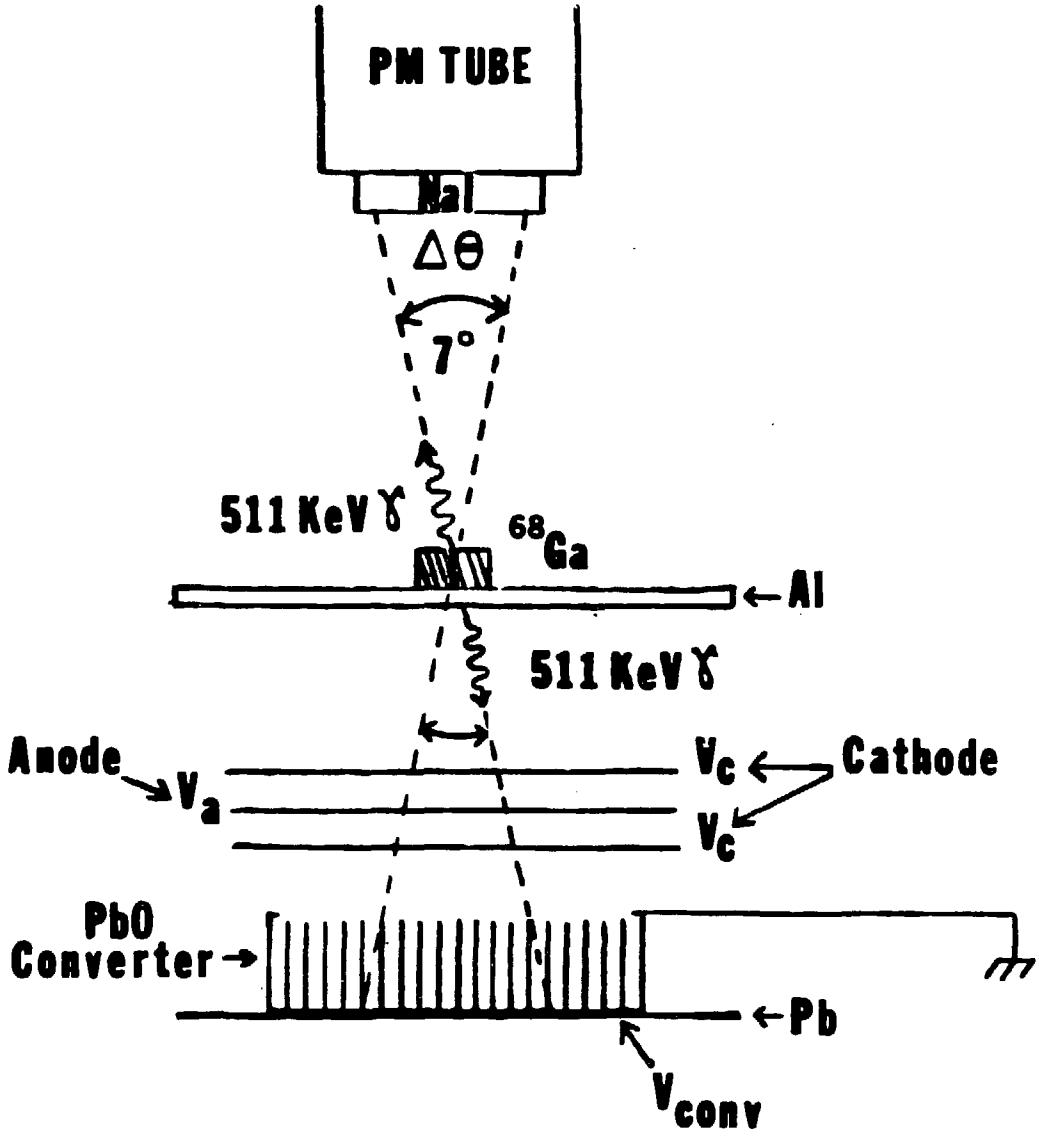
PM TUBE
Na
Δθ
7°
511 KeV γ
68Ga
Al
511 KeV γ
Anode
Va
Vc
Cathode
Vc
PbO
Converter
Pb
Vconv
XBL 822-8087

FIGURE 1

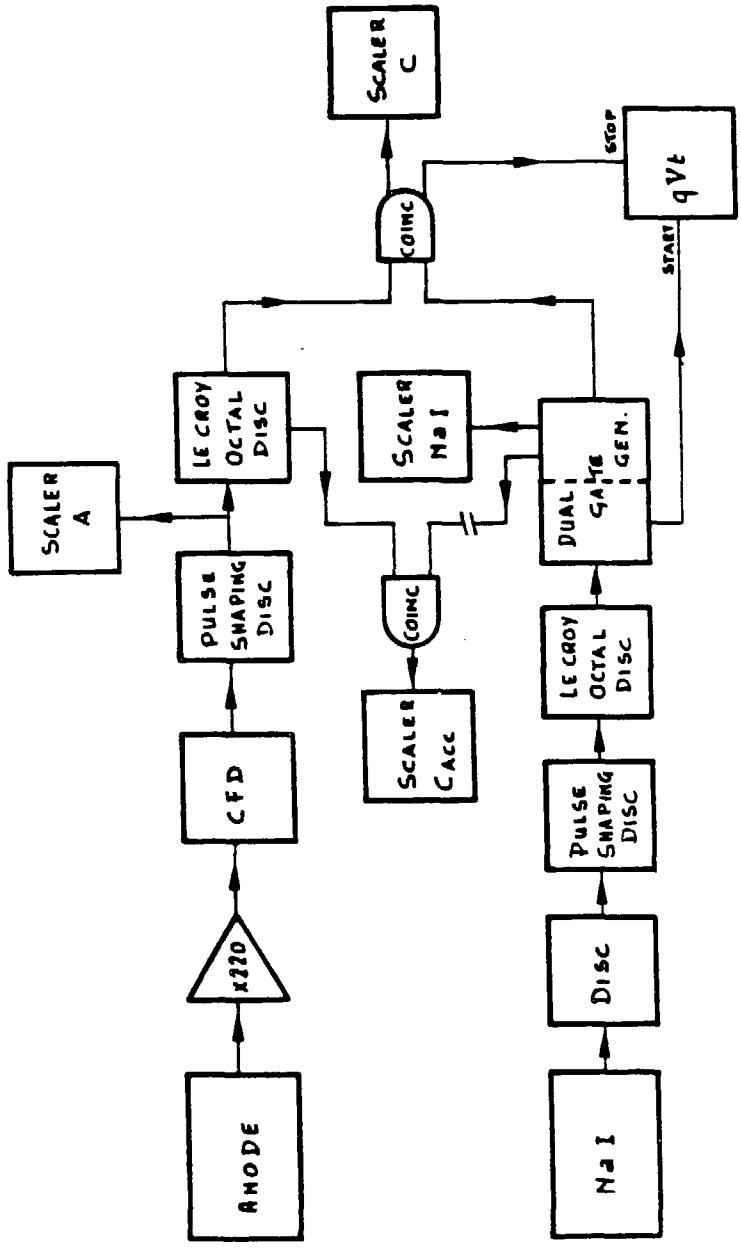
SCALER C
COINC
STOP
qVt
START
LE CROY OCTAL DISC
SCALER NaI
DUAL GATE GEN.
SCALER A
PULSE SHAPING DISC
COINC
SCALER CACC
LE CROY OCTAL DISC
CFD
PULSE SHAPING DISC
x220
DISC
ANODE
NaI

FIGURE 2

A

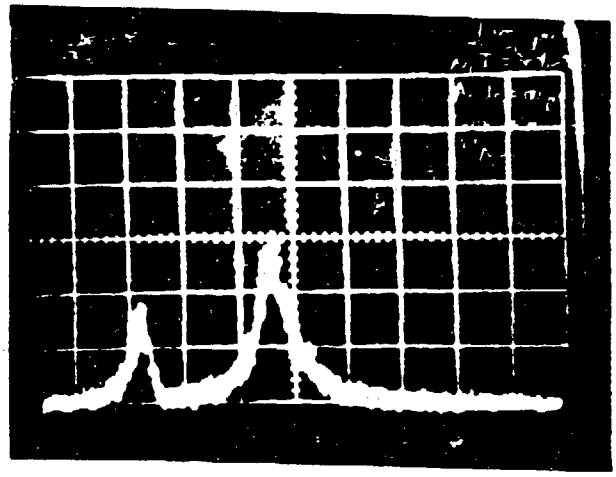

B

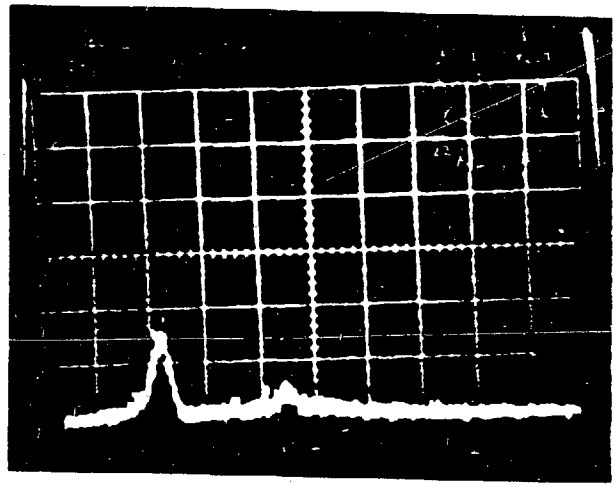

C

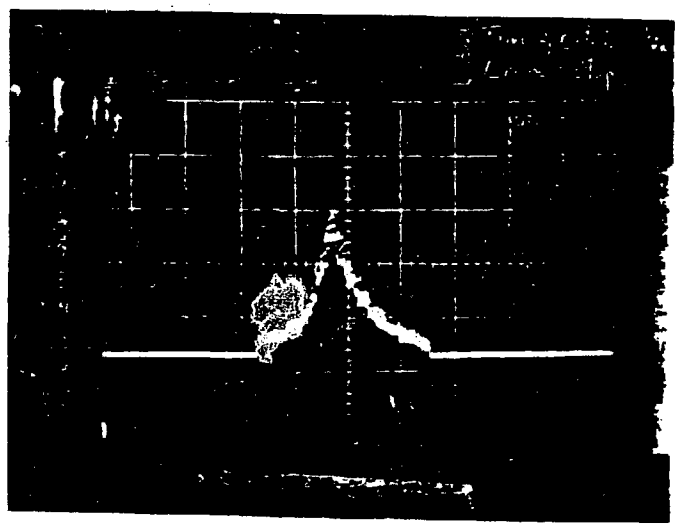

XBB 840-9232

FIGURE 3

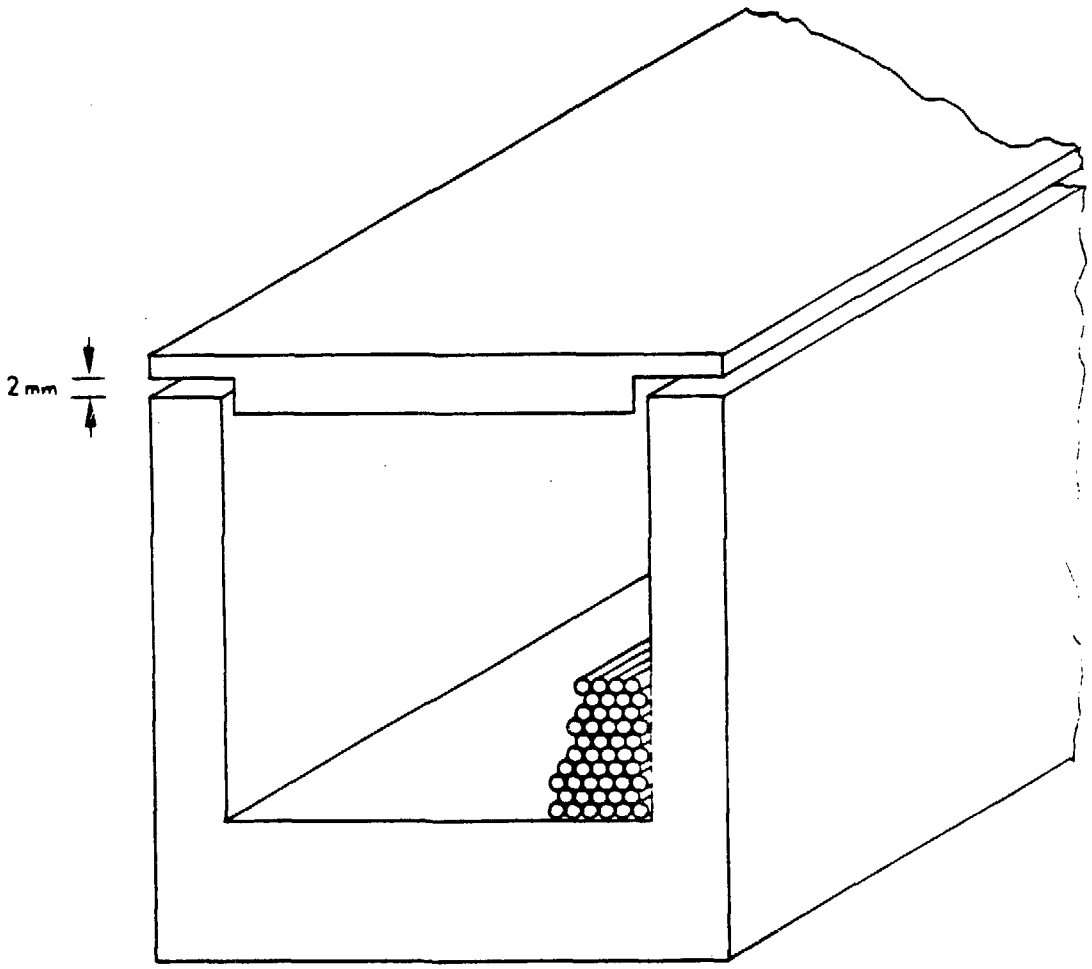

FIGURE 4

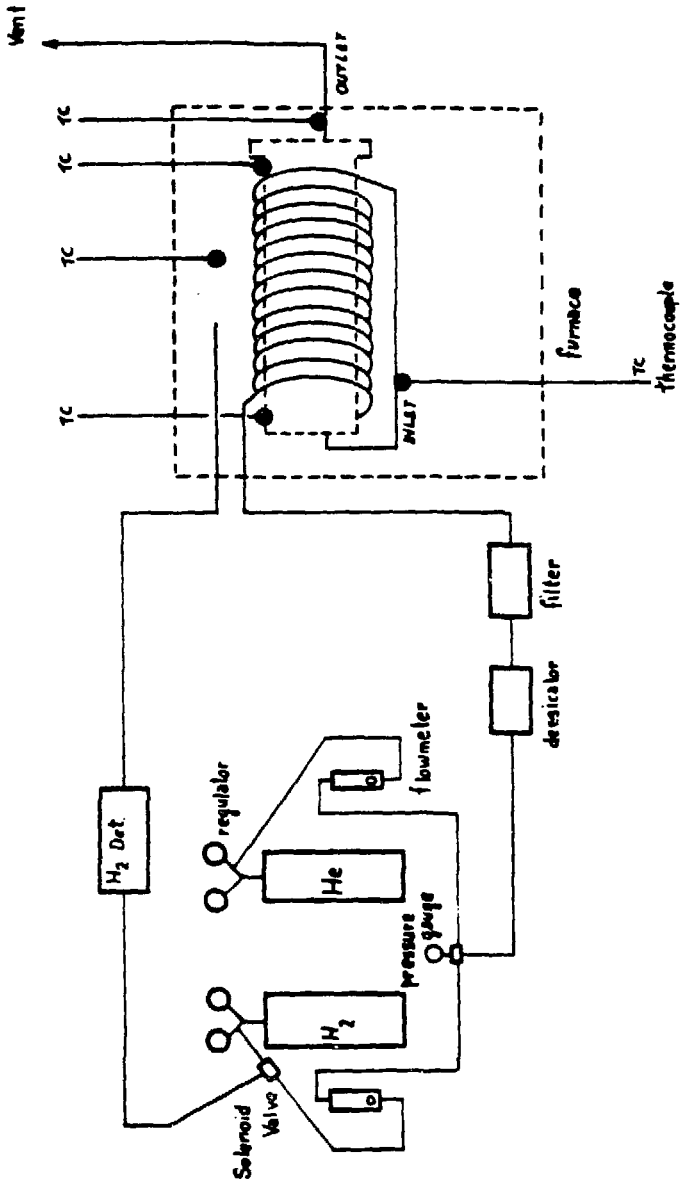
Vent
OUTLET
TC
TC
TC
TC
INLET
furnace
TC
thermocouple
filter
desicator
flowmeter
regulator
H_2 Det
He
pressure gauge
H_2
Solenoid Valve

FIGURE 5

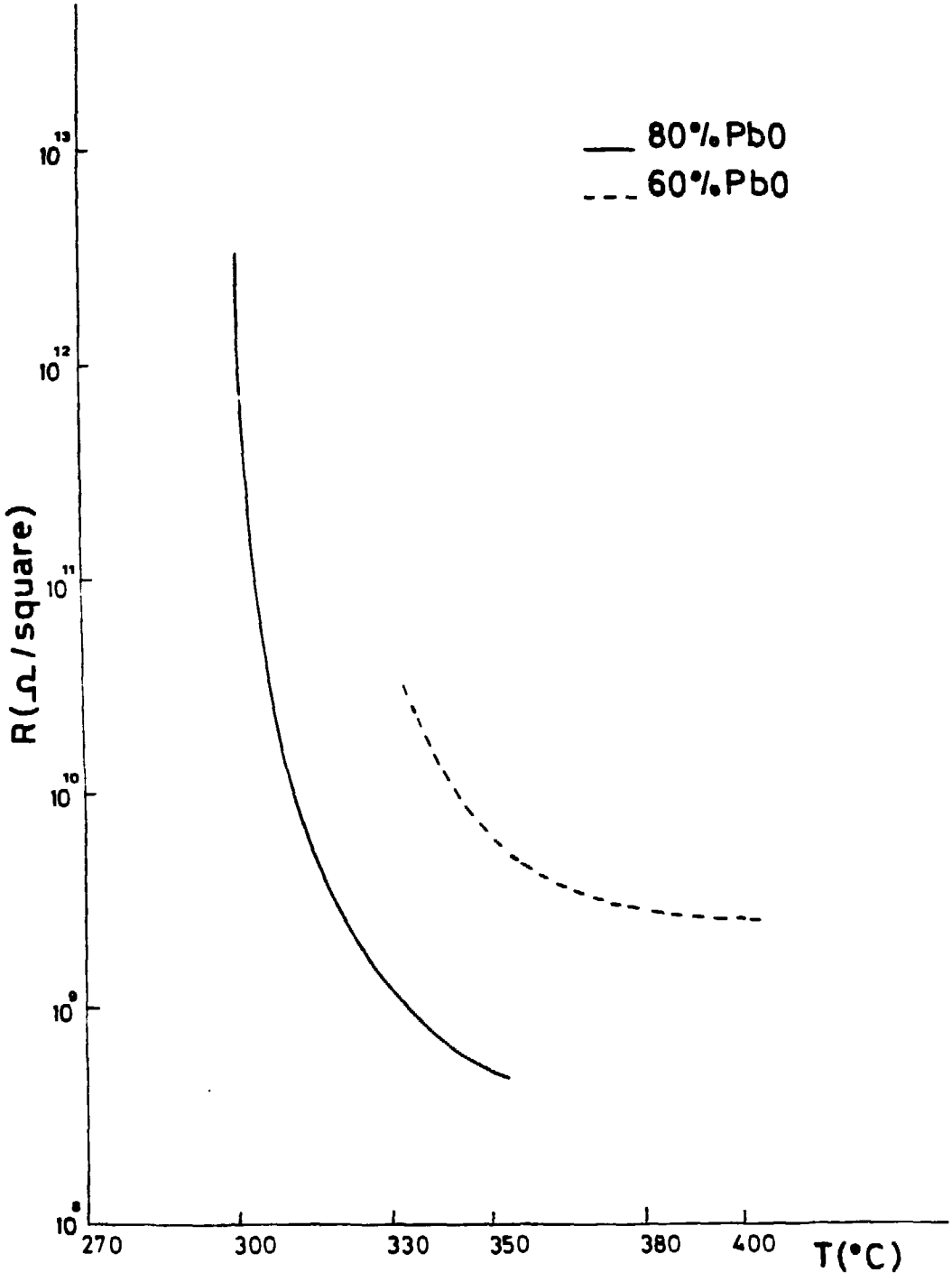
80%PbO
60%PbO
R(Ω/square)
10^13
10^12
10^11
10^10
10^9
10^8
270
300
330
350
380
400
T(°C)

FIGURE 6

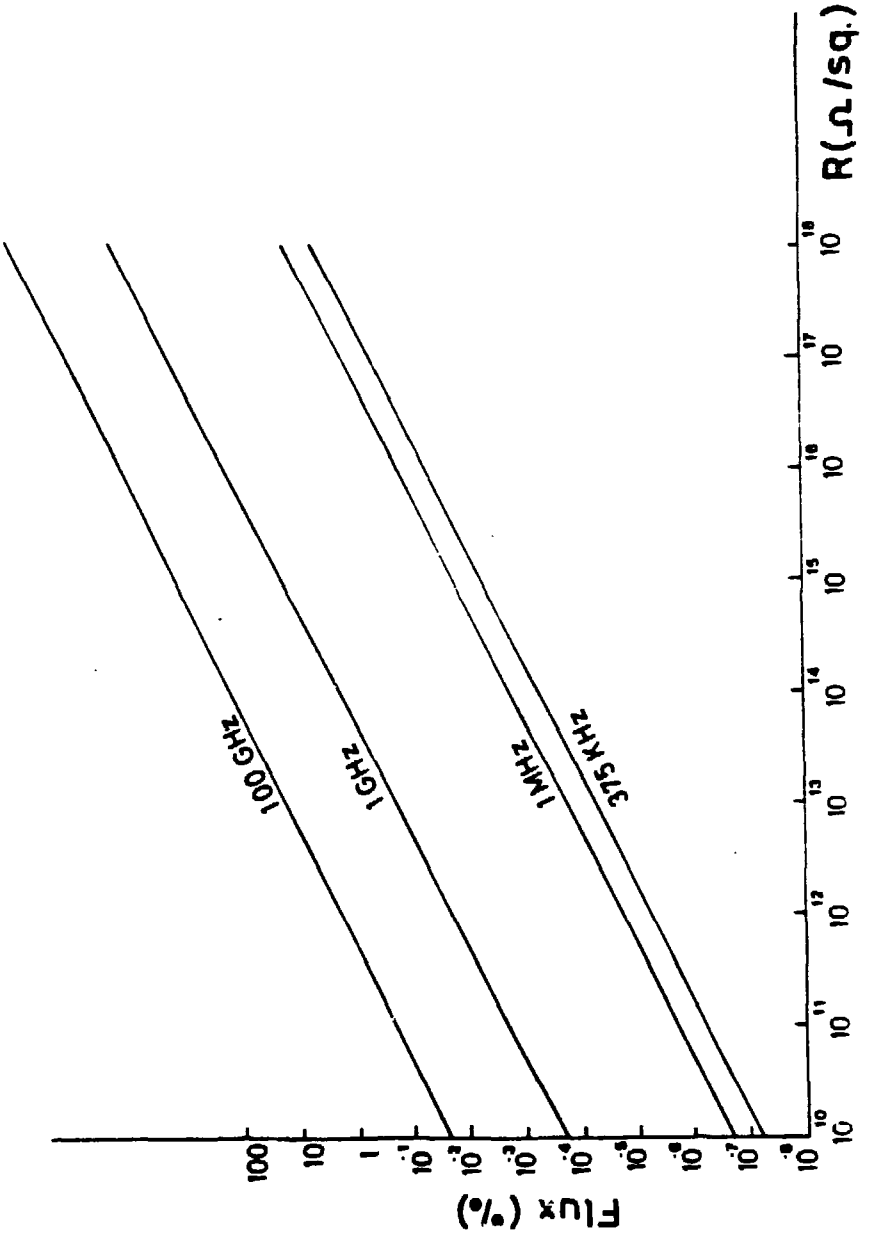

FIGURE 7

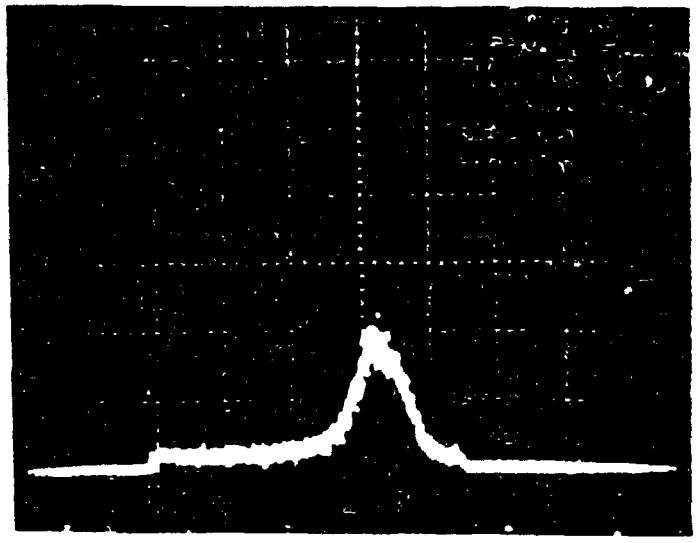

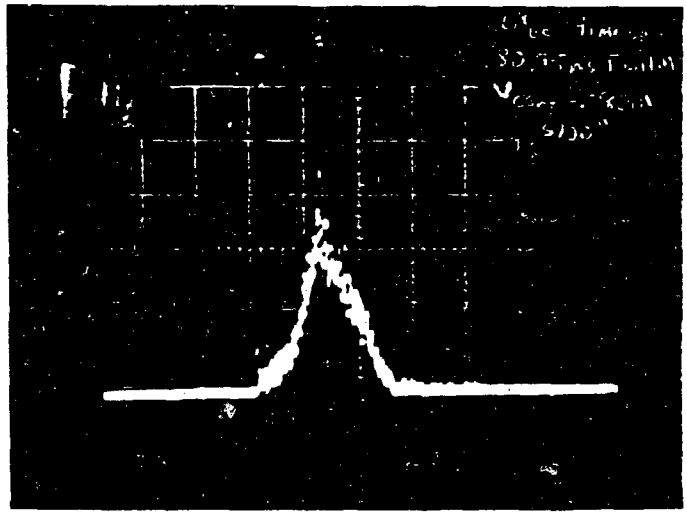

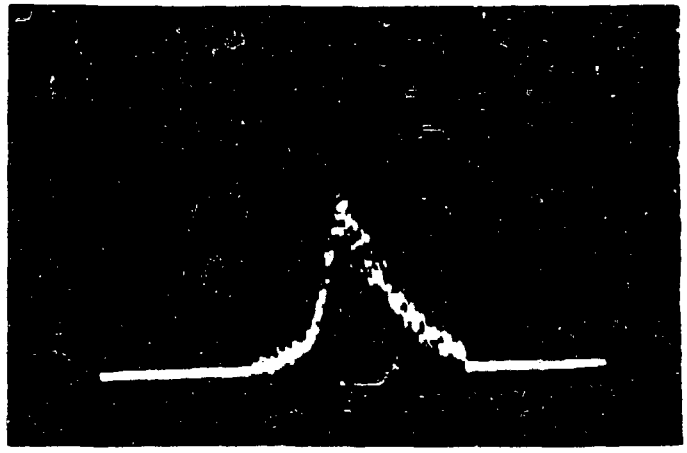

XBB 840-9233

FIGURE 8

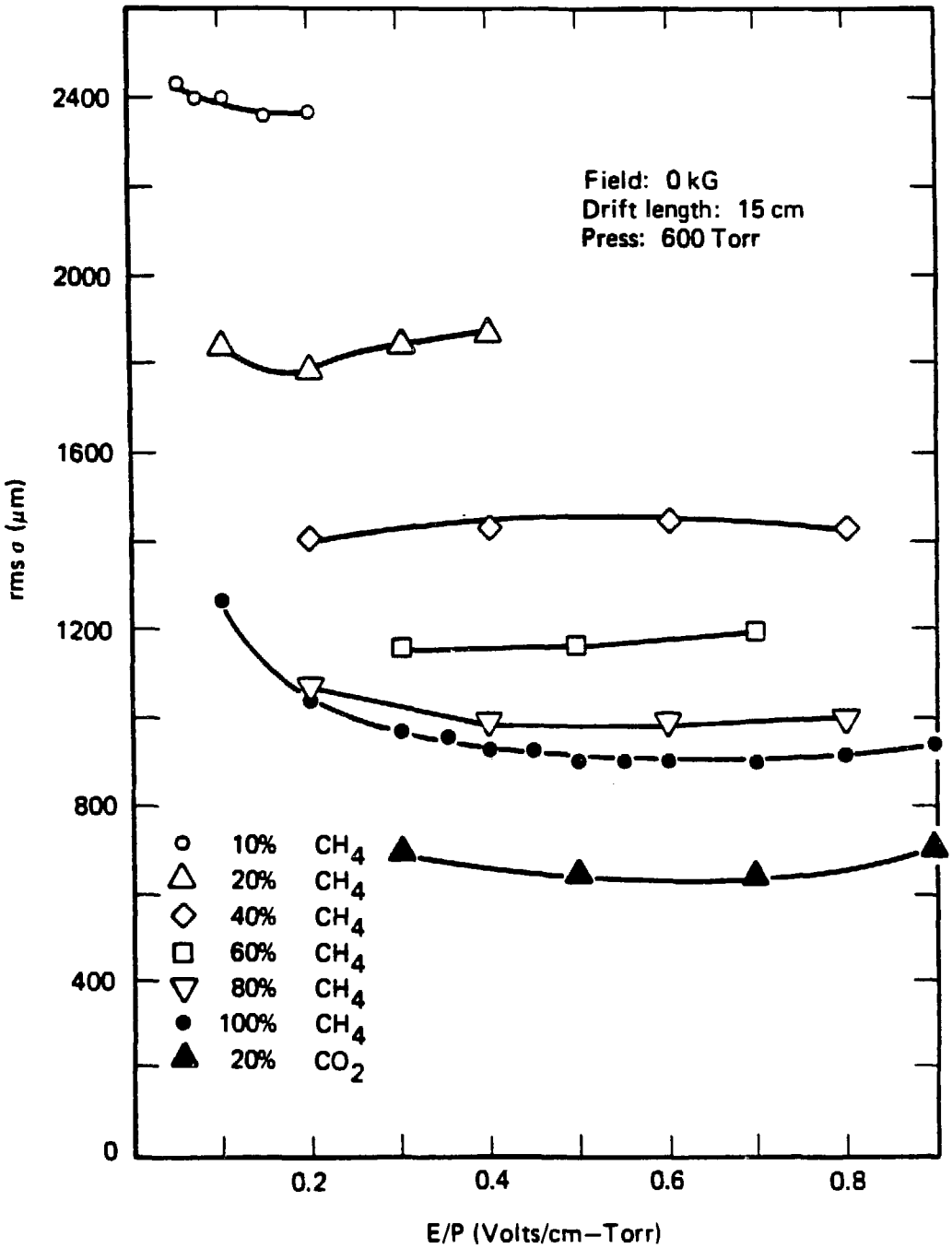

XBL 7512-9780

FIGURE 9

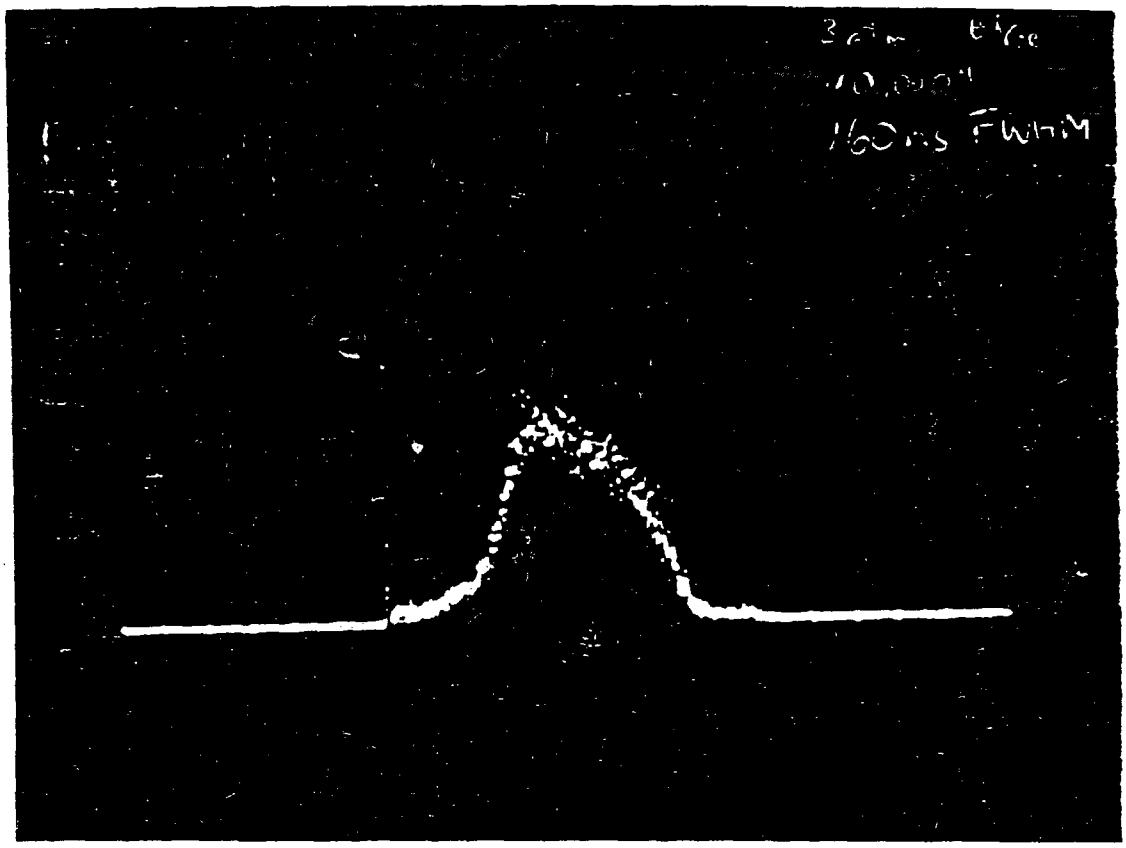

XBB 840-9237

FIGUPE 10

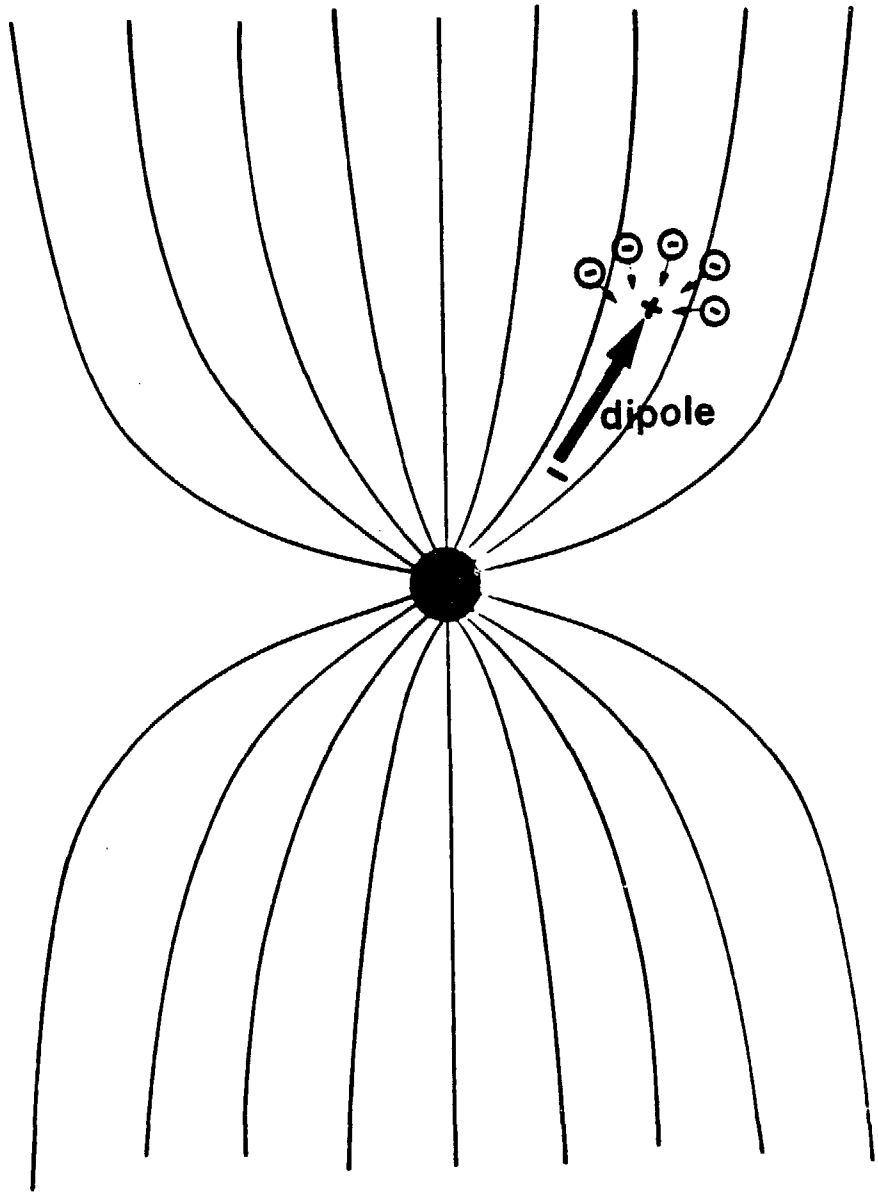

FIGURE 11

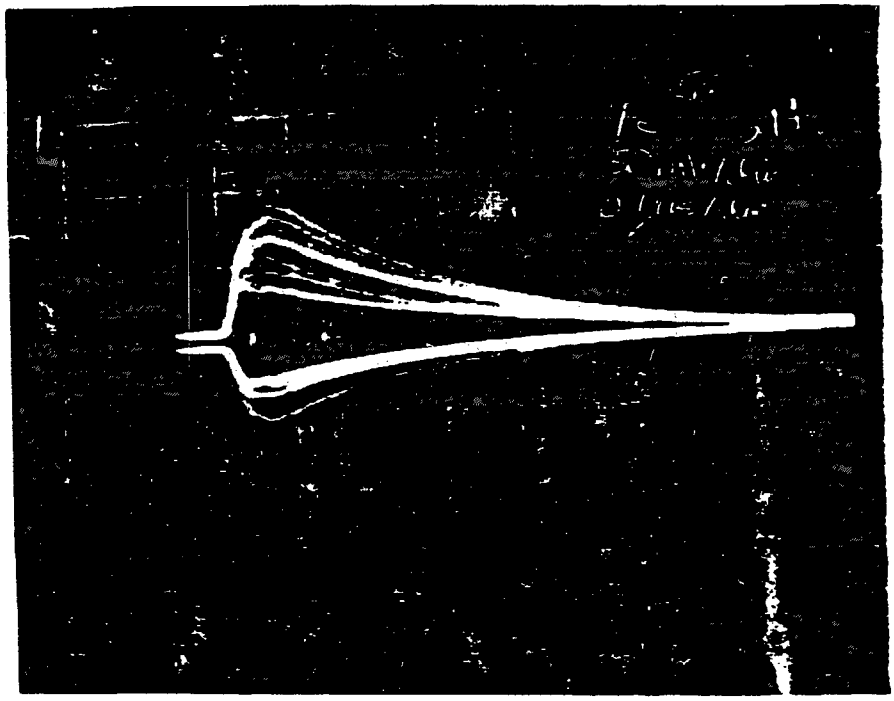

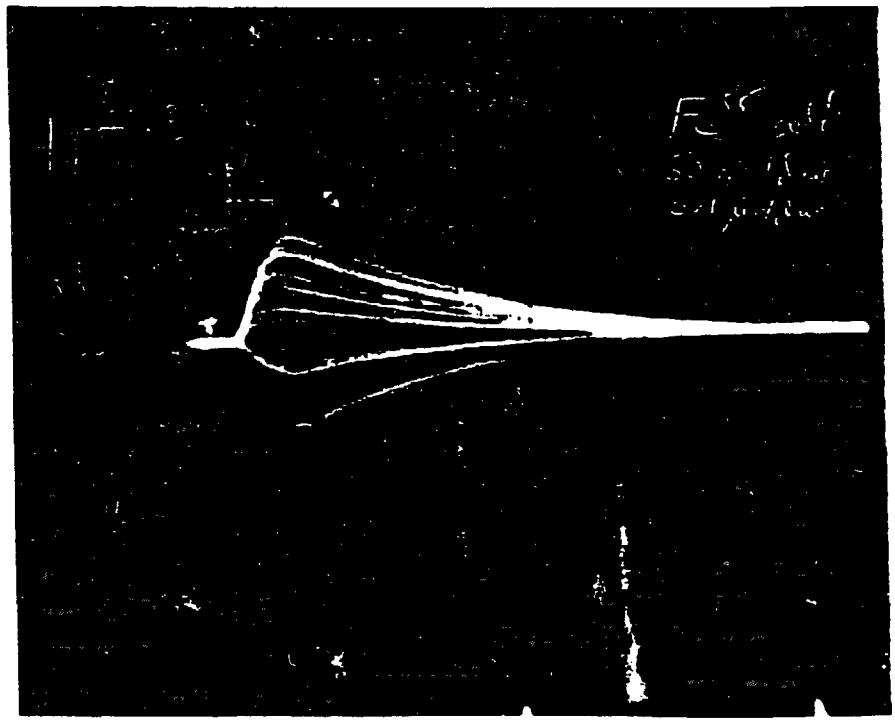

XBB 840-9235

FIGURE 12

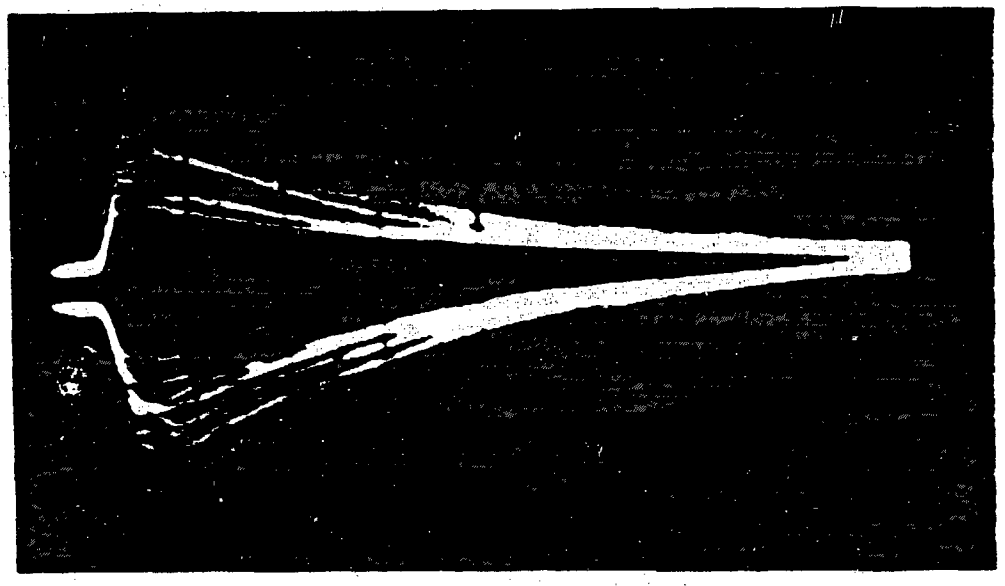

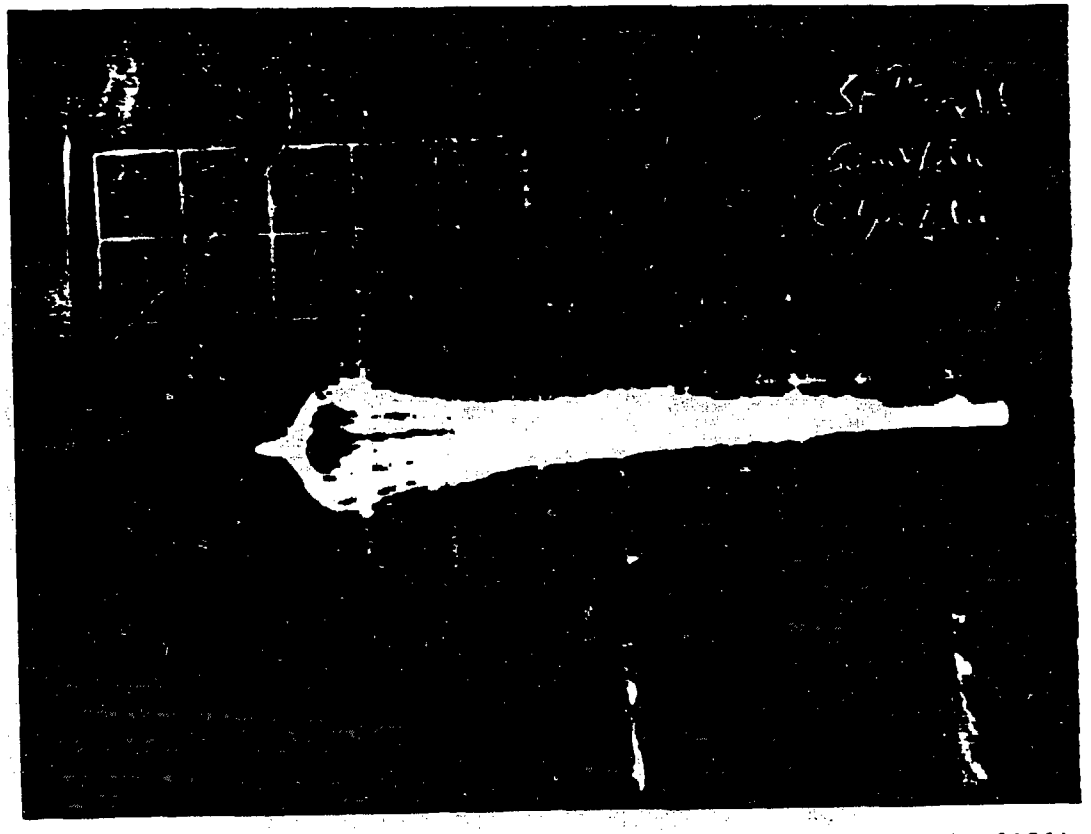

XBB 840-9236A

FIGURE 13

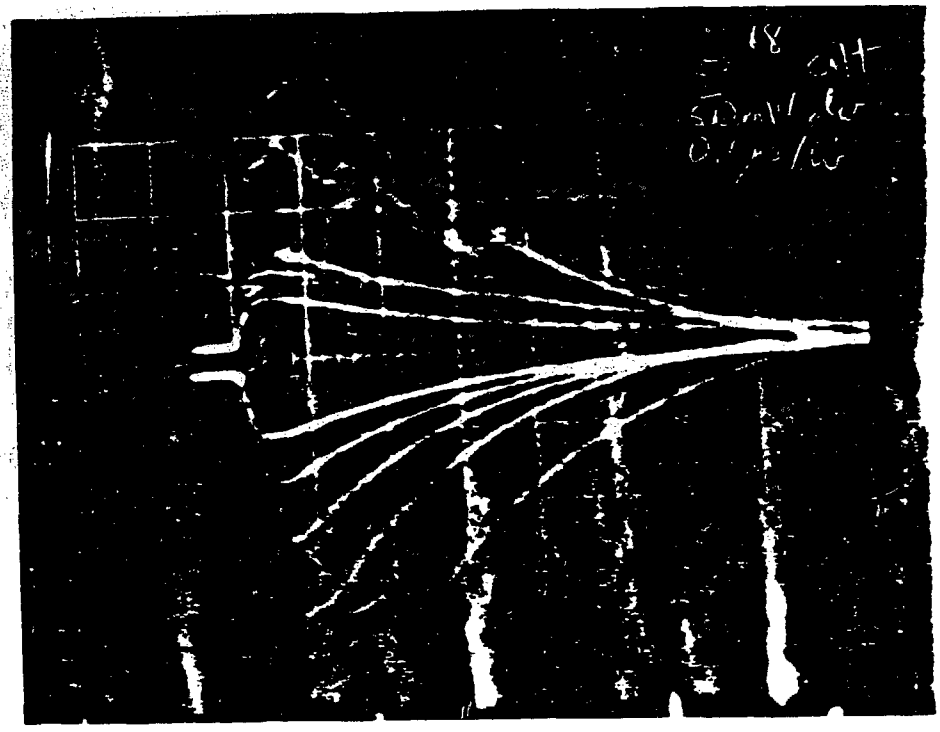

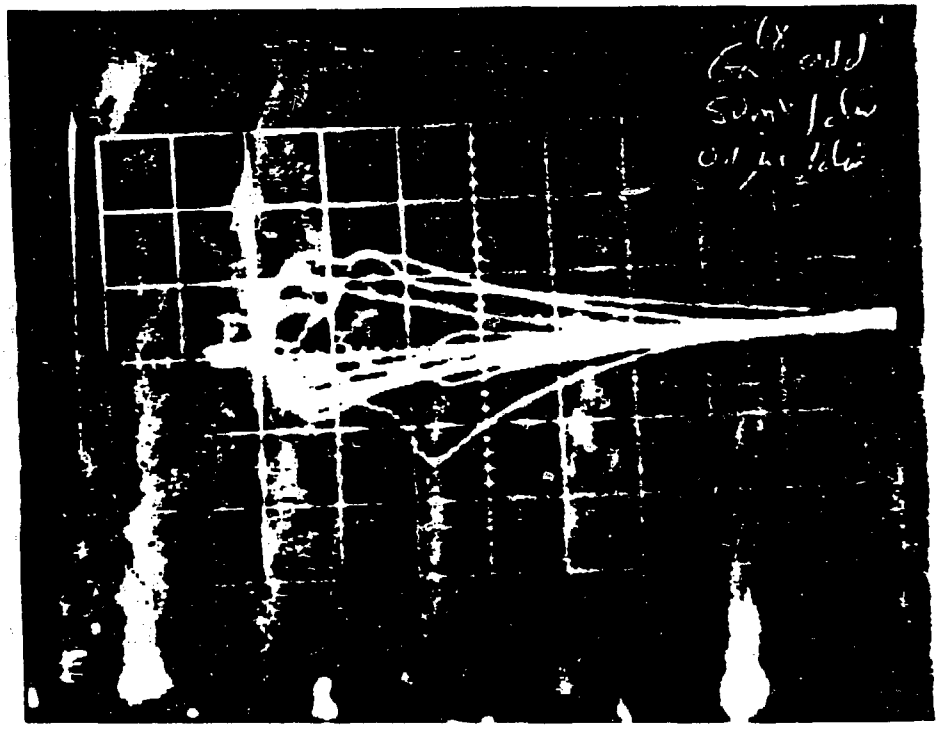

XBB 840-9234

FIGURE 14

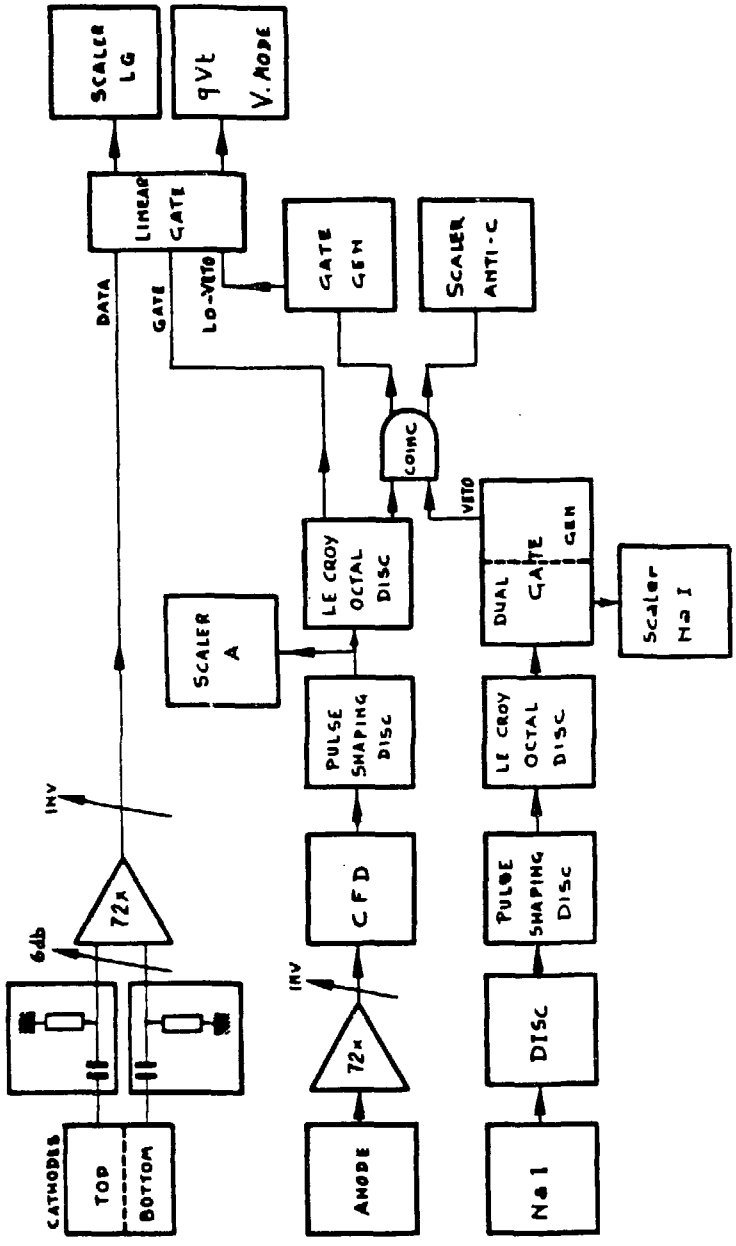
SCALER LG
qVt V. Mode
LINEAR GATE
DATA
GATE
LO-VETO
GATE GEN
SCALER ANTI-C
COINC
VETO
LE CROY OCTAL DISC
DUAL GATE GEN
Scaler No 1
SCALER A
PULSE SHAPING DISC
LE CROY OCTAL DISC
INV
72x
6db
C F D
PULSE SHAPING DISC
INV
72x
DISC
CATHODES
TOP
BOTTOM
ANODE
No 1

FIGURE 15

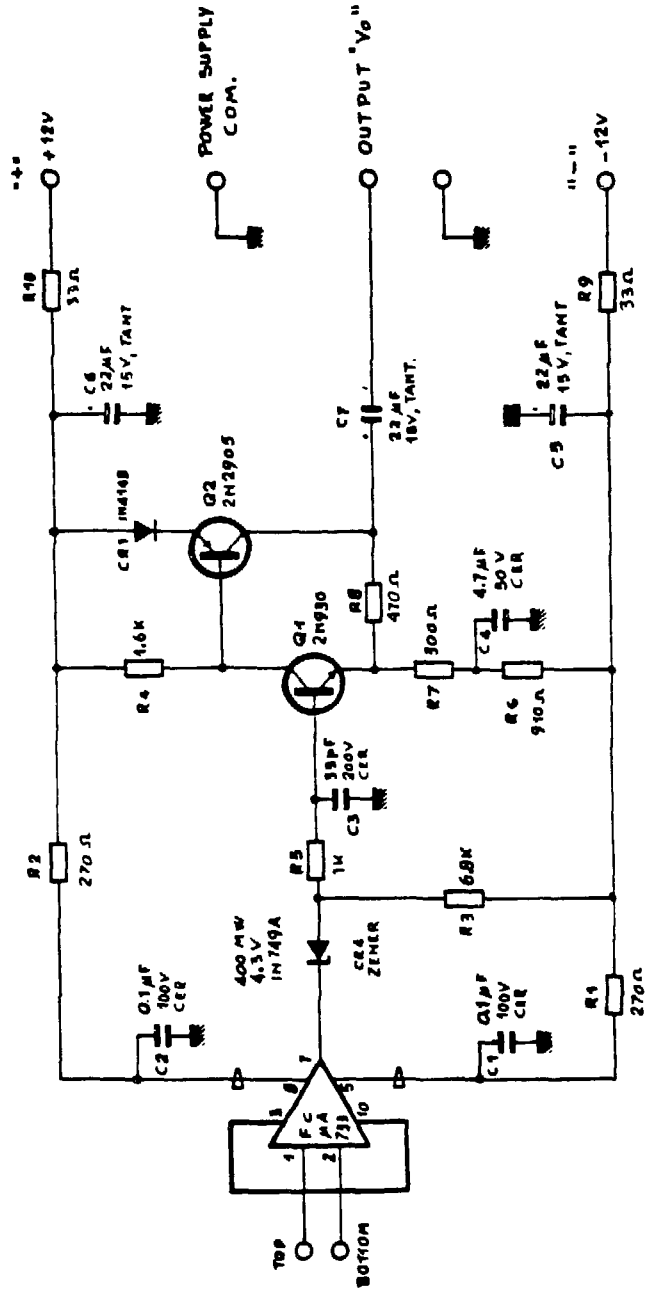
POWER SUPPLY COM.
OUTPUT "Vo"
+12V
-12V
R10 33Ω
R9 33Ω
C6 22μF 15V, TANT
C8 22μF 15V, TANT
C7 22μF 15V, TANT.
CR1 1N4148
Q2 2N2905
Q1 2N930
R8 470Ω
C4 4.7μF 50V CER
R4 1.6K
R7 300Ω
R6 910Ω
C3 33pF 200V CER
R2 270Ω
R5 1K
R3 6.8K
CR2 400 MW 4.3V 1N749A
CR4 ZENER
C2 0.1μF 100V CER
C1 0.1μF 100V CER
R1 270Ω
FC μA 733
TOP
BOTTOM

FIGURE 16

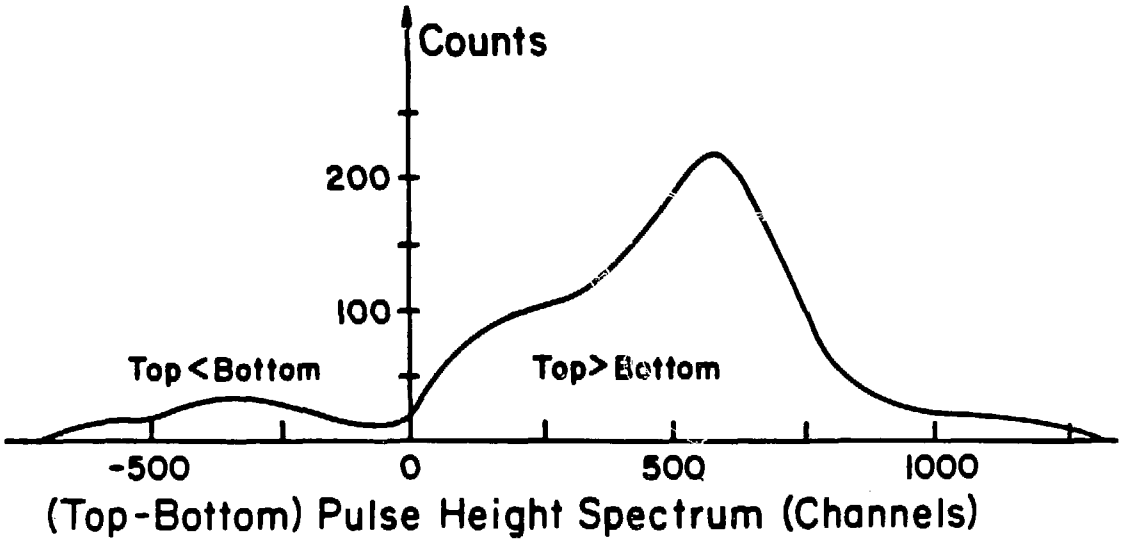

XBL 8210-2864

FIGURE 17

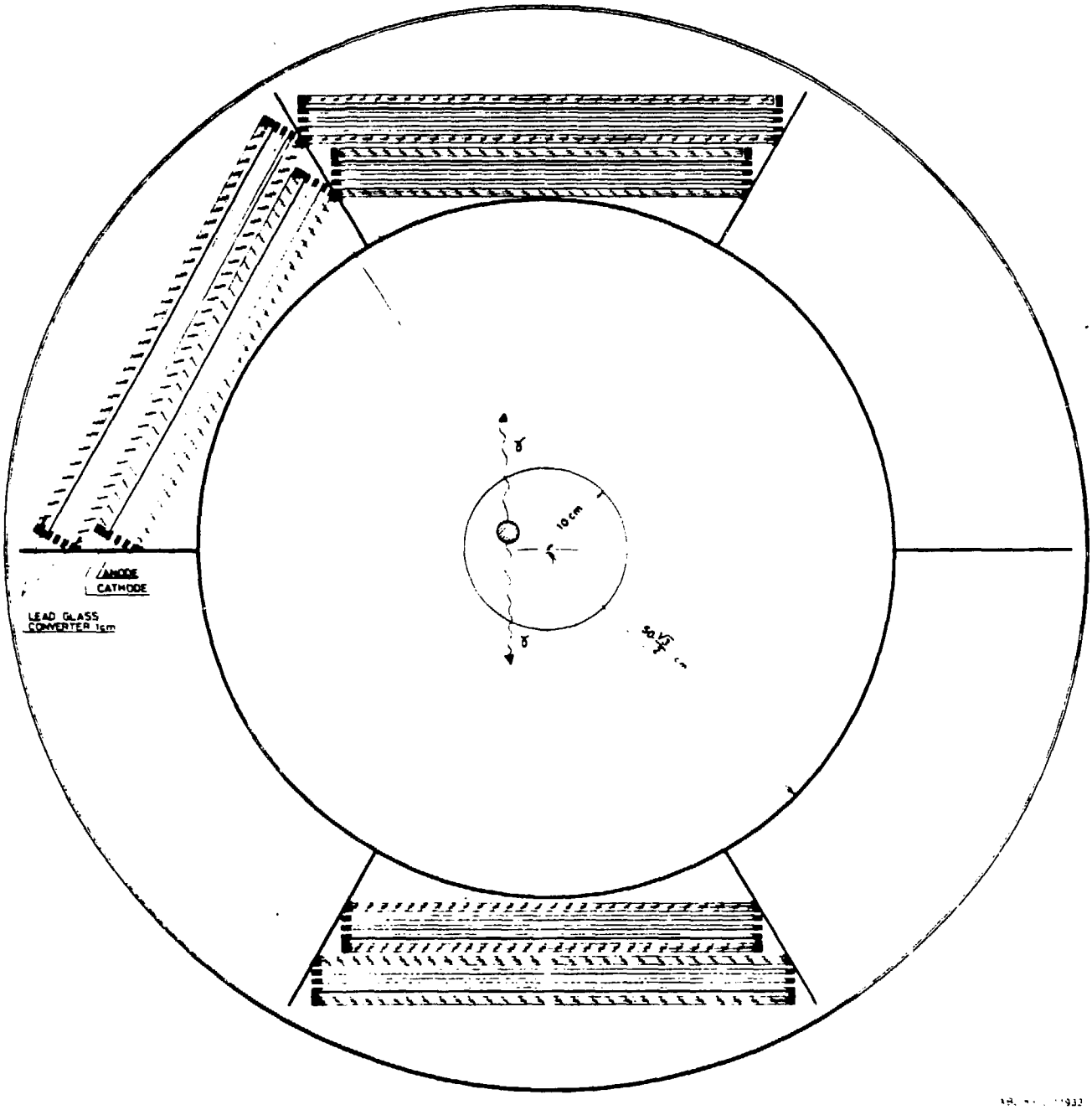

FIGURE 18

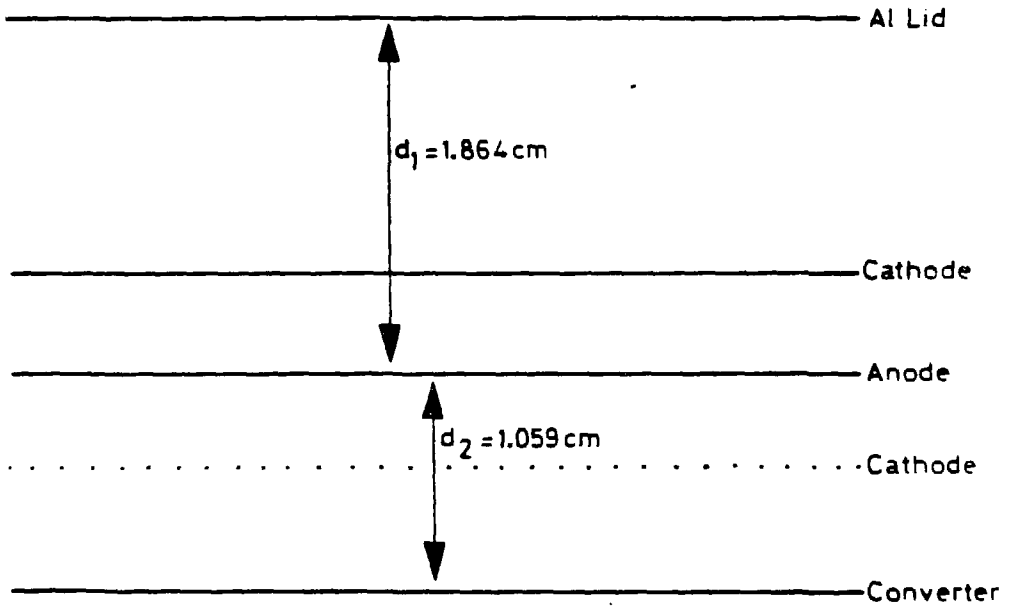

FIGURE 19

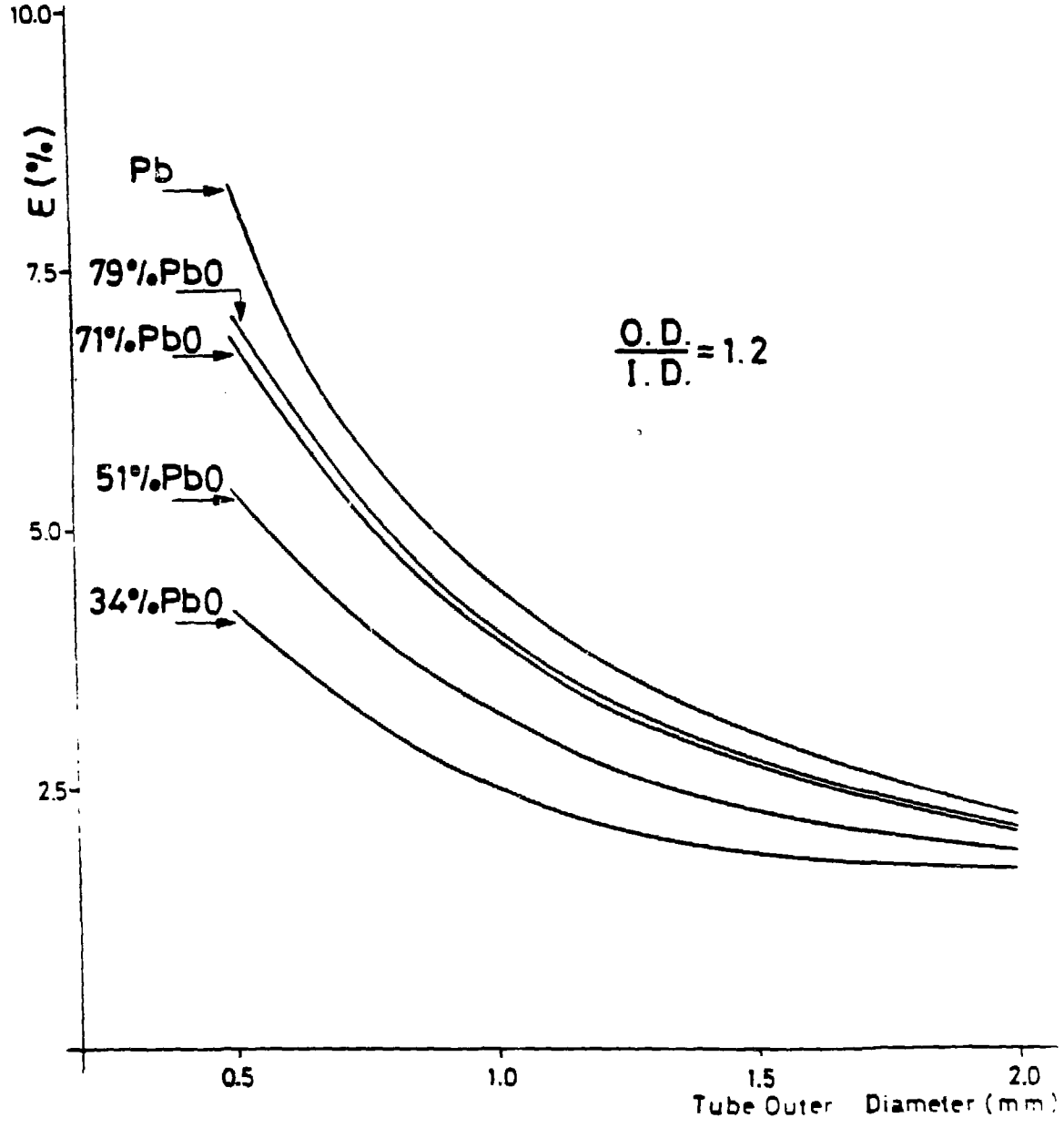
10.0
7.5
5.0
2.5
ε (%)
Pb
79%PbO
71%PbO
51%PbO
34%PbO
O.D./I.D. = 1.2
0.5
1.0
1.5
2.0
Tube Outer Diameter (mm)

FIGURE 20

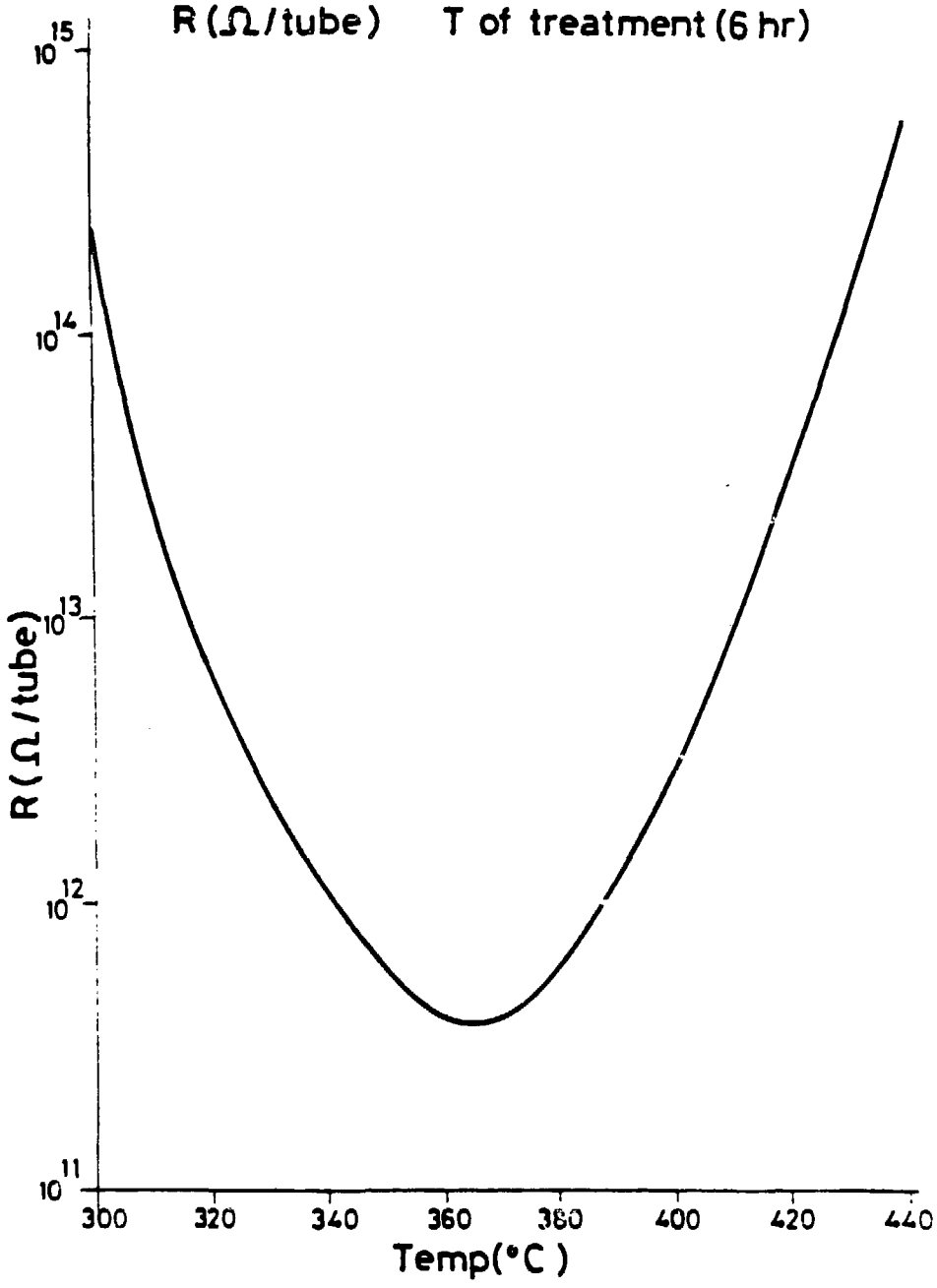
R (Ω / tube)
T of treatment (6 hr)
10^{15}
10^{14}
10^{13}
10^{12}
10^{11}
R (Ω / tube)
300
320
340
360
380
400
420
440
Temp(°C)

FIGURE 21

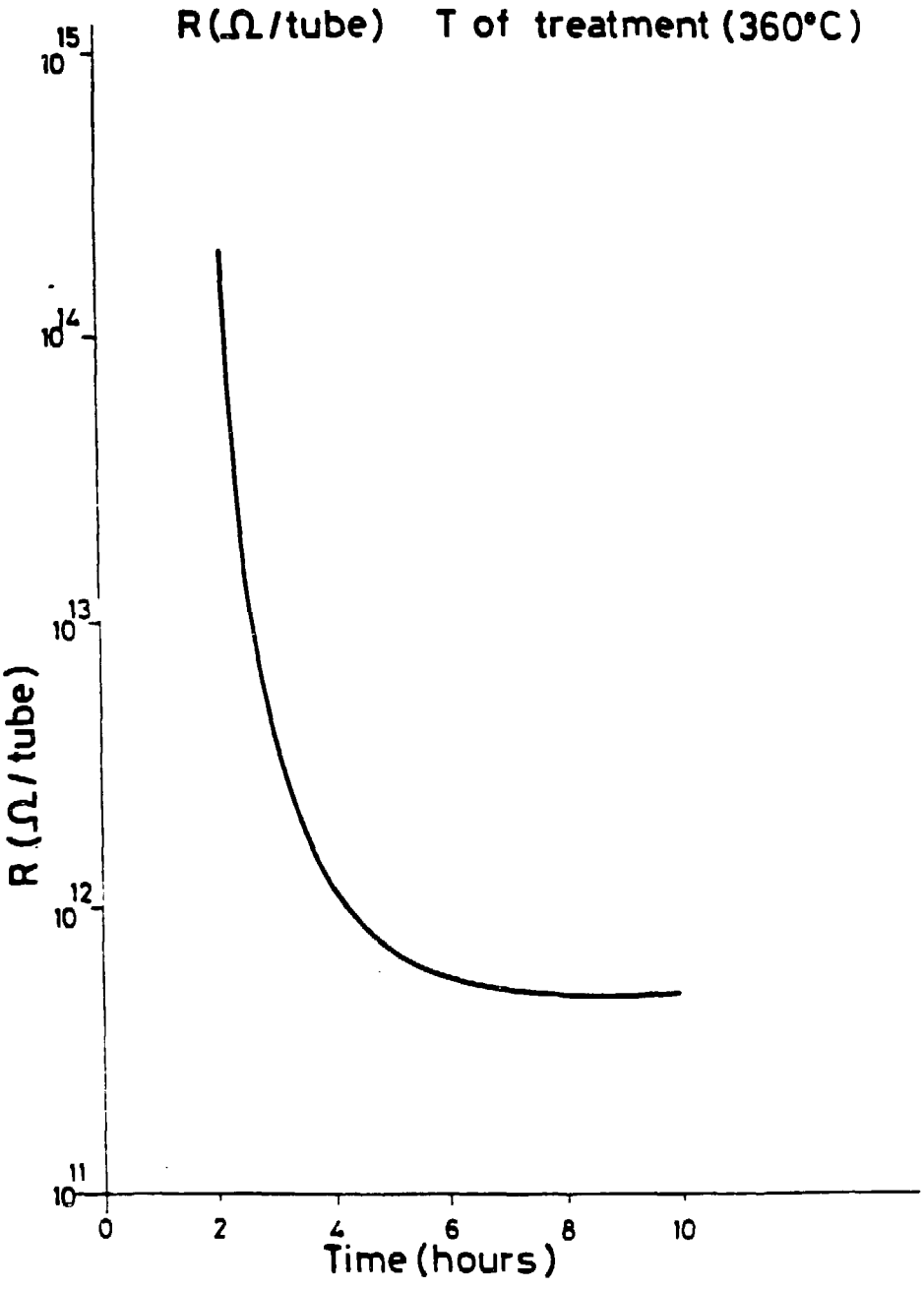
R(Ω/tube) T of treatment (360°C)
R (Ω/tube)
10^{15}
10^{14}
10^{13}
10^{12}
10^{11}
0
2
4
6
8
10
Time (hours)

FIGURE 22